Loss of the MLL3 tumor suppressor accelerates breast tumor onset via HIF1α-induced CCL2-mediated recruitment of CCR2$^+$ regulatory T cells

Marie Boutet[1†], Piril Erler[2,3†], Kenta Nishitani[2,3], Nicole Couturier[1], Zheng Zhang[2,3], Emeline Barbieux[1], Erik Guillen[1], Masako Suzuki[4], Gregoire Lauvau[1†*] and Wenjun Guo[2,3†*].

[1]Albert Einstein College of Medicine, Department of Microbiology and Immunology, Bronx, NY 10461, USA
[2]Albert Einstein College of Medicine, Department of Cell Biology, Bronx, NY 10461, USA
[3]Albert Einstein College of Medicine, Ruth L. and David S. Gottesman Institute for Stem Cell and Regenerative Medicine Research, Bronx, NY 10461, USA
[4]Albert Einstein College of Medicine, Department of Genetics, Bronx, NY 10461, USA

[*]**Correspondence to GL or WG:**
GL: Albert Einstein College of Medicine, Department of Microbiology and Immunology, 1301 Morris Park Avenue, Bronx, NY, 10461, USA. Ph: +1 718 678 1188, Fax: +1 718 678 1085, E-mail: gregoire.lauvau@einsteinmed.edu
WG: Albert Einstein College of Medicine, Department of Cell Biology, Ruth L. and David S. Gottesman Institute for Stem Cell and Regenerative Medicine Research, Albert Einstein College of Medicine, Bronx, NY 10461, USA. Ph: +1 718 678 1276, Fax: +1 718 678 1018, E-mail: wenjun.guo@einsteinmed.edu

[†]These authors contributed equally.

One Sentence Summary: MLL3 loss promotes tumorigenesis by enhancing recruitment of regulatory T cells.

Abstract

Understanding how specific cancer mutations modulate the tumor microenvironment is essential for developing new precision cancer therapies. The histone methyltransferase MLL3 is a tumor suppressor that is frequently mutated together with p53 and PI3-kinase in breast cancer. Herein, using a mouse mammary-stem-cell-based tumor model and CRISPR gene editing, we recapitulated this genetic setting and revealed that *Mll3* loss promotes tumorigenesis through enhancing tumor-intrinsic aggressiveness and establishing an immunosuppressive microenvironment. Specifically, HIF1α was upregulated in *Mll3*-mutant tumors and controlled proliferation and stem cell activity of the tumor cells. HIF1α also transcriptionally upregulated expression of the chemokine CCL2 by tumor cells. CCL2 further contributed to rapid CCR2-dependent accumulation of activated, proliferative KLRG1^{+}Foxp3^{+} regulatory T (T_{reg}) cells at very early stages of tumor initiation, promoting faster tumor onset. These results link MLL3 loss to HIF signaling, CCL2 and Treg cells, and the establishment of an early immune-suppressive microenvironment, a finding that may open new therapeutic opportunities for MLL3-mutant cancers.

Introduction

The relationship between tumor cells and the immune system is complex and involves multiple mechanisms. The concept of cancer immunoediting has been proposed as a framework to account for the processes resulting in the formation of established tumors and subsequent cancer progression [1,2]. Perhaps the most critical step in this model is when tumors have accumulated enough cancer driver mutations to breach the equilibrium and escape the immune response. It is well established that cancer driver mutations provide escaping tumor cells with intrinsic features that enhance their proliferative, migratory and survival potentials. However, how specific tumor mutations also alter the immune response to promote faster tumor onset and growth is an area that requires further investigations. Multiple immune mechanisms promote tumor growth. These include notably the recruitment and differentiation of immunosuppressive cells, such as myeloid-derived suppressor cells (MDSCs), type-2-polarized tumor associated macrophages ("M2-like TAMs") or regulatory T (T_{reg}) cells that exert their effects through secretion of intratumoral cytokines, chemokines, tumor cell growth factors or expression of checkpoint inhibitory receptors (i.e., PD-L1, PD-L2) [3-8]. Yet, only relatively few direct connections between cancer-driver mutations in cancer cells and their modulation of the immune response have been reported [9]. Some of these mechanisms link known cancer driver mutations (e.g., *TP53*, *MYC*, β-catenin pathway) and i) the upregulation of cell-surface checkpoint inhibitory receptors and innate immune regulators [10], ii) the modulation of MHC class I expression and NK-cell target ligands [11,12], iii) the increased secretion of chemokines and cytokines involved in the recruitment and differentiation of immune cells or receptors involved in tumor elimination [13-15]. These mechanisms differ depending on the mutational profile of the tumor, therefore it is paramount to achieve systematic understanding of these processes to design novel precision medicine strategies to eradicate distinct subtypes of tumors with various sets of cancer driver mutations.

Breast cancers remain the leading cause of cancer death in women despite significant improvement in early detection and treatment [16]. The 5-year survival rate for advanced breast cancers is only ~29% [17] Therefore, there is an urgent need for understanding molecular causes of breast cancers and for developing mechanism-based therapies. Currently, hormone therapy is used in treatment of hormone receptor positive (HR+) breast cancers while antibodies and kinase inhibitors targeting ERBB2 are used for HER2+ breast cancers. New targeted therapies, such as PI3K and CDK4/6 inhibitors, have also been approved for HR+ breast cancers. However, drug resistance often develops. Moreover, targeted therapy options fall short in treating triple-negative breast cancers (TNBC). Recently, immune checkpoint blockade (ICB) therapy has been approved for TNBC treatment, but only a small fraction of breast cancer patients respond to such therapy. Thus, a deeper understanding of the molecular determinants promoting tumor development and enabling suppression of anti-tumor immune response remains a necessity in breast cancer.

Genes encoding the histone methyltransferase MLL3 (also known as KMT2C) and the related COMPASS complex proteins, such as KMT2D and UTX, are among the most frequently mutated genes in various human cancer types [18-20]. Among these genes, *MLL3* is more frequently mutated in breast cancer, whereas *KMT2D* and *UTX* mutations occur at much lower frequencies[21-23]. Interestingly, the majority of *MLL3* mutations in breast cancer are truncating point mutations or gene deletions. Up to 27% of human breast cancers harbor loss of function mutations of MLL3 which correlate with poor prognosis in patients, but there is no clear bias towards specific breast

cancer subtypes. These data suggest that MLL3 is a tumor suppressor affecting a large percentage of breast cancers of all subtypes. Functional studies in mouse models and human cancer cell lines showed that the loss of MLL3 promotes tumor onset and growth in several cancer types, including breast, urethral and leukemia [24-27]. However, the mechanisms by which MLL3 suppresses tumor onset remain poorly defined. To date, MLL3 has been implicated in cell type-specific gene expression during differentiation, such as adipogenesis, myogenesis and macrophage activation. In breast cancer cell lines, MLL3 has been reported to regulate estrogen receptor (ER)-mediated transcription [28,29] . Yet, the high mutation rate of MLL3 in ER-negative breast cancer subtypes suggests that MLL3 controls tumorigenesis through other unknown mechanisms that remain to be elucidated.

In this study, we created a preclinical mouse model of breast cancer by genetically engineering mammary stem cells (MaSCs) to harbor the frequently associated cancer driver mutations *Pi3kca, Trp53*^{KO} (P5) or *Pi3kca, Trp53*^{KO} and *Mll3*^{KO} (MP5). Modified MaSCs were next implanted in mammary fat pads to investigate the role of Mll3 in tumorigenesis. We report that the loss of Mll3 promotes faster tumor onset and growth via tumor cell-intrinsic and extrinsic mechanisms. *Mll3*-mutant compared to *Mll3*^{WT} tumors acquired higher proliferative and stem-cell features and promoted HIF1α-mediated transcription of the chemokine CCL2. CCL2 contributed to rapid CCR2-dependent infiltration of Foxp3^{+} KLRG1^{hi} T_{reg} cells at very early stages of tumor initiation, accelerating *Mll3*-mutant tumor onset. These results represent a first step towards understanding MLL3-mediated regulation of the immune microenvironment in breast cancer, and likely other cancers where functional MLL3 is lost.

RESULTS

Loss of *Mll3* cooperates with Pik3ca activation and *Trp53* deletion to drive tumor initiation and growth

We previously established that *Mll3* deletion alone is insufficient to drive tumor initiation [27], suggesting the need for combining this mutation with other clinically relevant cooperating mutations to study *Mll3* loss in breast cancer. Thus, to define the most frequent mutations associated with *MLL3*, we first analyzed patient data from the MSKCC-IMPACT Breast Cancer database containing 1237 patients [30]. This revealed that *PIK3CA* mutations were the most frequent co-occurring mutations in the *MLL3*-mutant tumors (47.3% of the cases). Furthermore, tumors with both *MLL3* and *PIK3CA* mutations most often harbored *TP53* mutations (34% of the cases) **(Fig. 1a)**. We next evaluated these triple-mutant patient tumors for hormone receptor and HER2 status, which often determine courses and availability of treatments. The triple-mutant tumors belonged to heterogenous subtypes of breast cancers, similar to the general breast cancer population [31], including Her2+ (24.5%), triple-negative (22.2%), and estrogen receptor positive (ER+) (54.3%), suggesting a non-subtype-restricted role of *MLL3* mutations in breast cancer **(Suppl. Fig. 1a).** Altogether, the analysis of these patient data suggests that *PIK3CA* and *TP53* mutations are clinically relevant cooperating mutations in *MLL3*-mutant breast cancers.

Next, using our previously established mammary stem cell (MaSC)-based genetically engineered mouse model (GEMM) approach [27], we generated MaSC-GEMMs carrying either only *Pik3ca* and *Trp53* mutations (P5) or all three mutations combined (MP5) to study the effect of MLL3 loss during tumorigenesis in a clinically relevant genetic setting. To do so, we isolated MaSCs from mice that carry a Cre-inducible constitutively active patient hotspot mutation *Pik3ca*^{H1047R} (FVB background) [32] or a constitutively active mutant *Pik3ca** (C57BL/6 background) [33], activated the mutant *Pik3ca* gene with an adenoviral Cre vector, and then sequentially knocked-out the *Trp53* and *Mll3* genes with lentiviral CRISPR **(Fig. 1b).** Both gene deletions and *Pik3ca* gene activation were validated by western blot, showing loss of p53 and MLL3 protein expression and upregulation of phospho-AKT which is a downstream target of Pik3ca (**Fig. 1c**). As expected, the MP5 cells showed decreased levels of histone H3 lysine 4 mono-methylation (H3K4me1) and lysine 27 acetylation (H3K27ac) compared to P5 cells, which are known functions of the MLL3 complex [18] **(Suppl. Fig. 1b, c)**.

We then tested the effect of MLL3 loss on tumor initiation and progression *in vivo* through orthotopic transplantation of P5 and MP5 MaSCs to mammary glands of syngeneic wild-type (WT) recipient mice matching the strain background of MaSCs (**Fig. 1d**). Injection of MP5 MaSCs led to much earlier tumor onset in comparison to P5 cells (**Fig. 1e**). Furthermore, MP5 tumor growth was significantly faster than that of P5 tumors. These results were confirmed across 5 pairs of independently engineered P5 and MP5 MaSC lines that expressed either the *Pik3ca*^{H1047R} mutation or *Pik3ca** [33]. On average, median tumor onset and volume doubling time were 2.3±0.7 and 2.9±1.1 fold faster in MP5 than P5 tumors, respectively **(Fig. 1e, Suppl. Fig. 1d)**. Thus, these experiments conducted on our model recapitulating human breast cancer genetic makeup established that the loss of MLL3, combined with the most frequent co-occurring mutations, loss of *Tp53* and activated *Pik3ca*, enhances tumor onset and growth.

MLL3 loss contributes to accelerated tumor initiation, in part, via a tumor cell-extrinsic effect on lymphocytes

Our MaSC-based tumor model evaluates the effect of MLL3 loss on tumorigenesis in immunocompetent hosts. To further investigate whether loss of MLL3 enhances tumor onset and growth via tumor cell-extrinsic mechanisms that involve T and B lymphocytes, we transplanted P5 and MP5 MaSCs into immunodeficient *Rag1*$^{-/-}$ or control immunocompetent WT mice (**Fig. 2a**). The median tumor onset difference was 32 days between P5 and MP5 tumors in WT host, which was reduced to 11 days when the tumors initiated in *Rag1*$^{-/-}$ mice **(Fig. 2b, Suppl. Fig. 2a)**. Transplantation into these mice reduced the tumor onset of P5 by 27 days while that of MP5 was only reduced by 6 days when compared to WT hosts. Thus, while P5 tumor onset was significantly accelerated in *Rag1*$^{-/-}$ mice, MP5 tumor onset was only slightly different between the two hosts. In contrast to onset, P5 tumor growth over ~25 days was comparable between WT and *Rag1*$^{-/-}$ mice, while MP5 tumors grew significantly faster in *Rag1*$^{-/-}$ mice **(Fig. 2c)**. Altogether, these results suggested that the suppression of adaptive anti-tumor immunity during tumor initiation contributes to the faster onset of *Mll3*-mutant tumors.

Foxp3^{+} regulatory T cells infiltrate *Mll3*-mutant tumors during tumor initiation

To gain insights on how MLL3 loss modulated T and/or B lymphocyte responses during tumor onset, we next characterized the composition of immune cells infiltrating P5 and MP5 tumors at very early stages of tumor formation using high dimensional spectral flow cytometry with a panel of 27 distinct markers that includes all major immune cell lineages (**Table S1**). WT mice were injected with P5 or MP5 MaSCs, which were allowed to grow for 20 and 10 days, respectively, until they formed 1-2 mm nodules that are prior to onset of palpable tumors (~3 mm) **(Fig. 2d)**. Pre-onset tumor nodules were isolated and dissociated for FACS analysis of immune cell infiltrates. We gated cells based on forward and side scatter, excluded cell doublets and focused on CD45^{+} hematopoietic-derived immune cells that either expressed the myeloid marker CD11b or not (**Suppl. Fig. 2b**). Next, we used both t-Distributed Stochastic Neighbor Embedding (t-SNE) and flow Self-Organizing Map (FlowSOM) tools for unsupervised clustering and dimensionality reduction, and the visualization of discrete cell subsets, their similarities and their relative proportions. T-SNE analysis revealed that the proportions of pre-onset tumor-infiltrating CD45^{+} leukocytes including lymphocytes (CD4^{+} T, CD8^{+} T, B and NK cells) and subsets of myeloid cells (granulocyte-derived CD11b^{+}Ly6G^{+}, monocyte-derived CD11b^{+}Ly6C^{hi}, and Ly6C/G^{neg}CX3CR1^{+}) were comparable between P5 and MP5 pre-onset tumor nodules (**Fig. 2e and Suppl. Fig. 2c**). Numbers of CD45^{+} cells and all various immune cell subsets were also equivalent in P5 and MP5 nodules **(Suppl. Fig. 2b, d, e)**. Most interestingly, however, our analysis revealed significantly higher proportions and numbers of Foxp3^{+} CD4^{+} regulatory T (Treg) cells in MP5 compared to P5 nodules (2-fold, **Fig. 2f)**. Immunofluorescence in transplant sections also confirmed the significant increase in Treg cells in MP5 compared to P5 nodules (**Fig. 2g**). Further immunophenotyping of Treg cells using a T cell focused panel and subsequent FlowSOM analysis highlighted a distinct pattern of subset distribution and abundance (**Fig. 2h**). Specifically, we noted that MP5-infiltrating Treg cells included more diverse and expanded subsets than P5-infiltrating Treg cells. In addition, some of the expanded subsets (dotted lines) in MP5 pre-onset tumor nodules were KLRG1^{hi}, ICOS^{hi}, PD-1^{hi}, CD44^{hi}, CD62L^{lo} and proliferating (Ki67^{hi}), consistent with a more activated and suppressive phenotype than those of P5 counterparts (**Fig. 2i**) [34-36]. Of

note, these expanded subsets of Treg cells also expressed Sca1, CD27, CD127 and CD11a, and ~half of them expressed the CD103 integrin that is associated with tumor residency (**Supp. Fig. 2f, g**) [37]. In various cancers including breast cancer, tumor-draining lymph nodes (dLNs) represent key sentinel nodes regulating the anti-tumor immune response [38]. Thus, we also evaluated the immune cell composition and activation status in dLNs of P5 and MP5 pre-onset tumor-bearing mice (**Suppl. Fig. 2h, i**). Similar frequency and numbers of $CD4^+$ T, $CD8^+$ T, Treg and B cells were found, and Treg cells did not express KLRG1 or CD103, and exhibited lower ICOS and Ki67 expression, overall indicating that local cues in the early-stage tumor microenvironment were most likely to account for the observed differences in Treg cells.

Our results in Fig. 2c suggested that after onset, loss of MLL3 most likely enhances tumor growth via mechanisms other than those regulating adaptive anti-tumor immunity. We nevertheless assessed whether rapid MP5 tumor expansion was related to differences in T or B lymphocyte infiltration, we monitored these cells in later stage tumors (300-500 mm^3, **Supp. Fig. 2j**). Equivalent proportions and numbers of $CD8^+$ T, $CD4^+$ T, Treg and B cells between P5 and MP5 tumors were quantified. We also found comparable expression of various functional T cell markers (granzyme B, PD-1, CD103) among $CD4^+$ and $CD8^+$ T cells from P5 and MP5 tumors (**Suppl. Fig. 2k**). Thus, these data suggested that MLL3 loss may not enhance late-stage tumor growth by impacting T and B cells. In summary, the functional loss of MLL3 in tumor cells promotes rapid tumor initiation that is associated with an early infiltration and/or differentiation of activated proliferating $KLRG1^{hi}ICOS^{hi}$ $Foxp3^+$ Treg cells inside pre-onset tumor nodules that form rapidly after implantation.

MLL3 loss increases mammary stem cell activity and tumor cell proliferation in a cell-intrinsic manner

Since implanting MaSCs in *Rag1*$^{-/-}$ mice did not fully rescue the difference between P5 and MP5 tumor onset and did not restore tumor growth at all, we next investigated the tumor cell-intrinsic processes that contributed to the effects of MLL3 loss on tumorigenesis. We assessed cell proliferation and death in pre-onset tumor nodules and in large tumors formed by injecting P5 and MP5 MaSCs in WT recipients. The frequency of $Ki67^+$ cells in MP5 pre-onset tumor nodules was ~2-fold higher than in P5 nodules, consistent with the faster onset of MP5 tumors **(Fig. 3a)**. Furthermore, large MP5 tumors retained 2-fold higher $Ki67^+$ cell frequencies than P5 tumors of similar sizes (**Fig. 3b**). In contrast, apoptosis, as measured by cleaved caspase 3, was comparable between P5 and MP5 samples both at pre-onset and large-tumor stages **(Suppl. Fig. 3a, b)**. To further determine if the higher proportion of proliferating cells was a cell-intrinsic feature of MP5 tumor cells, we isolated P5 and MP5 tumor cells from exponentially growing tumors (~100 mm^3) and grew them in organoid culture to directly evaluate the growth of P5 and MP5 tumor cells *ex vivo*. While both cell types formed organoids at comparable frequencies, MP5 tumor organoids proliferated faster and contained substantially higher cell numbers **(Fig. 3c)**. We also directly measured organoid growth of P5 and MP5 MaSCs **(Fig. 3d)**. We observed that MP5 MaSCs showed significantly augmented organoid formation, an *in vitro* assay for MaSC activity [27,39]. Interestingly, MP5 MaSC organoids could grow largely independent of exogenous EGF, FGF2 and serum, while these factors were necessary for efficient formation of P5 MaSC organoids **(Fig. 3e, Suppl. Fig. 3c)**. Thus, collectively, loss of MLL3 increased stem and tumor cell proliferative capacities making them more independent from growth factors.

HIF1α contributes to the early onset of *Mll3*-mutant tumors

We previously established that *Mll3* deletion in WT MaSCs results in activation of the HIF1α pathway [27]. We confirmed that HIF1α target genes, such as *Vegfa*, *Glut-1*, *CaIX*, *Timp1* and *Adm* [40,41], were also expressed at higher levels in MP5 than P5 MaSCs (3-10 fold), as determined via qRT-PCR analysis on multiple independent MaSCs lines, also suggesting that the effect of MLL3 on HIF1α activation is not bypassed by *Pik3ca* and *Trp53* mutations (**Fig. 4a, Suppl. Fig. 4a**). As shown above, we observed increased stem cell activity both in medium supplemented with growth factors and in the base medium. HIF1α target gene transcripts were also upregulated in MP5 MaSCs cultured without EGF and FGF2 compared to P5 MaSCs (**Suppl. Fig. 4b**). Similarly, by analyzing the TCGA dataset, we found well-characterized HIF1a target genes such as *VEGFA* and *GLUT1* to be significantly upregulated in tumors with *MLL3* mutations (**Suppl. Fig. 4c**). Thus, we next investigated whether loss of *Mll3* upregulated the HIF1α pathway *in vivo* by comparing P5 and MP5 pre-onset tumor nodules and large tumors. Immunohistochemistry analysis of pre-onset tumor nodules revealed a marked upregulation of HIF1α expression in MP5 nodules compared to P5 nodules of the same size, an effect consistent for two pairs of independently engineered MaSCs lines (**Fig. 4b, Suppl. Fig. 4d**). Interestingly, in large tumors resulting from the same two pairs of lines, both P5 and MP5 tumor cells expressed high levels of HIF1α, suggesting that MLL3-independent mechanisms increase HIF1α expression in late-stage P5 tumors (**Suppl. Fig. 4e**).

We next assessed whether the upregulation of the HIF1α pathway contributed to the increased cell proliferation in MP5 MaSCs. We first compared the effect of hypoxia on P5 and MP5 MaSC organoids, by culturing the cells at 1% oxygen to induce HIF1α expression [42](**Fig. 4c**). We found that hypoxia rescued organoid-forming efficiency and cell proliferation in P5 MaSCs to similar levels as in MP5 MaSCs, whereas it had no significant effect on MP5 MaSCs. To further assess the requirement of HIF1α in MP5 cells, we utilized lentiviral CRISPR to delete *Hif1a* in MP5 MaSCs and validated the deletion by western blot (**Suppl. Fig. 5a**). *Hif1a* deletion in MP5 cells (MP5-sg*Hif1a*) significantly reduced the organoid-forming efficiency and cell proliferation compared to control MP5 cells expressing a non-targeting guide RNA (MP5-sgNT) (**Fig. 4d**). Organoid formation and proliferation in MP5-sg*Hif1a* was similar to that of P5-sgNT MaSCs. These results suggested that activation of the HIF1α pathway in MP5 cells is responsible for their increased proliferation compared to P5 cells.

To determine whether elevated HIF1α contributes to the accelerated initiation and growth of *Mll3*-mutant tumors, we transplanted MP5-sgNT and MP5-sg*Hif1a* MaSCs into WT recipient mice (**Fig. 5a, Suppl. Fig. 5b**). MP5-sg*Hif1a* MaSCs showed a significant delay in tumor onset compared to MP5-sgNT MaSCs (15 days, i.e., a ~63% delay) and MP5-sg*Hif1a* tumors were markedly smaller than MP5-sgNT tumors (~7 fold) when measured 30 days post-transplantation (**Fig. 5b**). Altogether, these results indicated that *Mll3* deletion promotes stem cell activity and tumorigenesis at least in part through the upregulation of HIF1α.

Treg cell infiltration of *Mll3*-mutant tumors is HIF1α-dependent

We next investigated whether the difference in Treg cell infiltration between P5 and MP5 pre-onset tumor nodules is also regulated by the increased levels of HIF1α in *Mll3*-mutant tumors. P5-sg*NT*, MP5-sg*NT* and MP5-sg*Hif1a* MaSCs were transplanted into WT mouse fat pads, and tumors and draining lymph nodes analyzed by FACS 20, 10 and 10 days later, respectively, when the three types of cells form similar sized pre-onset nodules (**Fig. 5c**). We noted lower frequencies (~3 fold less) and numbers (~2 fold less) of Treg cells in MP5-sg*Hif1a* and P5-sg*NT* nodules compared to MP5-sg*NT* (**Fig. 5d**). Moreover, the proportion of tumor-infiltrating non-Treg $CD4^+$ T cells was higher in P5 tumors while the overall numbers were comparable in all nodules, indicating that loss of HIF1α more specifically alters Treg cells compared to other $CD45^+$ leukocytes including $CD8^+$ T cells (**Supp. Fig. 5c**).This result was also confirmed by immunofluorescence on sections of pre-onset tumor nodules, showing significantly fewer $CD4^+Foxp3^+$ Treg cells in MP5 tumors lacking HIF1α (MP5-sg*Hif1a*) compared to control tumors (MP5-sg*NT*), and proportions were also comparable to P5-sg*NT* tumors (**Fig. 5e)**. Of note, the numbers and proportion of $CD4^+$ T cells, Treg cells, and $CD8^+$ T cells in tumor dLNs were not significantly different between the different groups (**Fig. 5f and Supp. Fig. 5d**). Thus collectively, these results indicated that HIF1α favors Treg cell infiltration and/or differentiation in the MP5 pre-onset tumor nodules.

HIF1α induces CCL2 in the tumor cells and CCL2 contributes to early tumor onset and Treg cell infiltration in *Mll3*-mutant tumors

We hypothesized that cytokines and/or chemokines in the *Mll3*-mutant tumor microenvironment promoted Treg cell recruitment and/or differentiation. Using a multiplex bead-based array, we screened a panel of 26 cytokines/chemokines commonly involved in immune-cell function and tumor growth, and quantified their amounts in P5-sg*NT*, MP5-sg*NT* and MP5-sg*Hif1a* pre-onset tumor nodules (**Supp. Fig. 6a**). While we noted that the levels of several cytokines and chemokines were significantly different between the P5 and MP5 nodules, CCL2 was the only one also exhibiting a substantial diminution in HIF1α-deficient MP5 tumors (**Fig. 6a**). Similarly, *Ccl2* mRNA levels were consistently lower in P5 compared to MP5 MaSCs, for all independent cell lines generated (**Supp. Fig. 6b**). We then tested P5-sg*NT*, MP5-sg*NT* and MP5-sg*Hif1a* MaSCs, also revealing decreased *Ccl2* mRNA in MP5-sg*Hif1a* to levels that were comparable to that of P5-sg*NT* MaSCs (**Fig. 6b**). Together these results indicated that MLL3-deficient cells upregulated *Ccl2* mRNA and chemokine expression in a HIF1α-dependent manner. Since HIF1α promoted CCL2 expression, we next tested whether HIF1α bound to regulatory regions of the *Ccl2* gene (**Fig. 6c**). For this, we searched transcription factor binding motifs around the *Ccl2* gene region by CiiDER analysis and identified a HIF1β binding site within the first exon of *Ccl2*. Since HIF1β forms a heterodimer with HIF1α to activate target genes, this suggested HIF1α may bind to the same site. We also identified hypoxia response element (HRE) motifs near both the mouse and human *CCL2* gene transcription start sites (**Supp. Fig. 6c)**. In addition, we found three putative enhancer regions based on ENCODE annotation and two reported regulatory regions up- or downstream of the *Ccl2* transcription start site (TSS) [43,44]. We next performed HIF1α ChIP-qPCR in MP5 cells to determine whether HIF1α bound to any of these putative regulatory regions (**Fig. 6d**). Compared to gene desert regions used as negative controls, HIF1α was significantly enriched within three regions near the *Ccl2* TSS including the HIF1β binding site, indicating that HIF1α may act as a direct transcriptional regulator for *Ccl2* expression.

Consistent with our findings, we observed a positive correlation between *HIF1A* and *CCL2* mRNA expression in *MLL3*-mutant breast cancers in the TCGA patient data set (**Supp. Fig. 6d**).

To further explore whether CCL2 contributes to tumor development, we treated mice injected with MP5 MaSCs with anti-mouse CCL2 neutralizing or isotype control Abs (**Figure 6e and Supp. Fig 6e**). While anti-CCL2 Ab treatment significantly delayed MP5 tumor onset by ~10 days compared to isotype control treated group, tumor growth was comparable in both groups, indicating that CCL2 contributed to tumor initiation but not growth. Although the number of infiltrating leukocytes ($CD45^+$), $CD4^+$ T (non-Treg), $CD8^+$ T and B cells in MP5 tumor pre-onset tumor nodules of anti-CCL2 Ab-treated mice trended lower compared to isotype-Ab treated mice, only Treg cell numbers were significantly decreased (**Fig. 6f and Supp. Fig. 6f**). This result suggested that despite the broad impact of CCL2 neutralization on many infiltrating immune cells, Treg cells were more selectively unable to infiltrate pre-onset tumor nodules compared to other leukocytes. However, in contrast to the clear differences we reported in expanded subsets and the phenotype of Treg cells infiltrating MP5 versus P5 pre-onset tumor nodules (**Fig. 2i**), FlowSOM analysis of MP5-infiltrating Treg cells did not reveal any significant differences between anti-CCL2 and isotype Ab-treated mice (**Fig. 6g**). Collectively, these results established that CCL2, derived from tumor cells and likely other cells, enables more selective infiltration and expansion of Treg cells inside pre-onset tumor nodules.

Lack of CCR2 impairs effective Treg cell recruitment and differentiation/expansion in the tumor microenvironment

Since CCL2 enables higher numbers of Treg cells in *Mll3*-mutant tumors, we predicted that if CCL2 mediated direct chemotaxis of Treg cells in pre-onset tumor nodules, $CD4^+$ Treg and/or possibly non-Treg cells lacking CCR2, the major receptor for CCL2, should fail to infiltrate the tumor nodules. To formally test this possibility, we generated mixed bone marrow (BM) chimeras in which WT B6 $CD45.1^{+/-}$ mice were lethally irradiated and reconstituted with a 1:1 ratio of WT ($CD45.1^{+/+}$) and $Ccr2^{-/-}$ BM (**Fig. 7a and Supp. Fig. 7a)**. The frequencies and numbers of WT and $Ccr2^{-/-}$ hematopoietic-derived ($CD45^+$) cells in blood and tumors were close to the reconstituting ratio (1:1). Most interestingly, the proportion and numbers of $Ccr2^{-/-}$ Treg cells were significantly lower than that of WT counterpart in tumor nodules while tumor-infiltrating non-Treg $Ccr2^{-/-}$ $CD4^+$ T cells were increased compared to WT counterparts (**Fig. 7b**). Thus, this result suggested that CCR2 mediated the competitive recruitment to pre-onset MP5 tumor nodules of Treg cells, and also possibly of non-Treg $CD4^+$ T cells that quickly differentiated into Treg cells once in the tumor nodules. $Ccr2^{-/-}$ Treg and non-Treg cell proportions and numbers in dLNs and non-dLNs were slightly increased yet remained comparable to WT counterparts (**Fig. 7c and Supp. Fig. 7b, c**). Altogether these data support the interpretation that the deficit of $Ccr2^{-/-}$ Treg cells in pre-onset tumors is most likely the result of an impaired recruitment of Treg cells but not of non-Treg $CD4^+$ T cells. Of note, both Treg and non-Treg $CD4^+$ T cells in dLNs expressed CCR2, consistent with the model that $CCR2^+$ Treg cells from dLNs infiltrate pre-onset tumor nodules via CCL2/CCR2-mediated chemotaxis **(Supp. Fig. 7d**). $Ccr2^{WT}$ Treg cells in the nodules also expressed higher levels of KLRG1 and of the marker of proliferation Ki67 than $Ccr2^{-/-}$ counterparts, while non-Treg $CD4^+$ T cells or dLN Treg cells did not express KLRG1 (**Fig. 7d and Supp. Fig 7e**). Collectively, these results suggested that $Ccr2^{WT}$ Treg cells infiltrated *Mll3*-mutant

tumors from the dLNs via CCL2 attraction, and quickly expanded (Ki67^{+}) and differentiated into KLRG1^{+} Treg cells.

DISCUSSION

In this work, we show that the functional loss of the MLL3 tumor suppressor protein has both cell-intrinsic and cell-extrinsic effects. MLL3 loss promoted tumor cell proliferation and stem cell activity, and increased expression of the transcription factor HIF1α inside the tumor cells. We further report that HIF1α induced secretion of the chemokine CCL2 by the tumor cells. HIF1α binds to the HRE-containing regulatory elements close to the *Ccl2* transcription start site, suggesting its transcriptional control of *Ccl2* expression. CCL2, most likely secreted from tumor cells, enables the rapid infiltration of Foxp3$^+$ Treg cells in *Mll3*-mutant pre-onset tumors. We establish that CCL2 mediated CCR2$^+$ Treg cell recruitment to the tumors where they expand and differentiate into activated KLRG1$^+$ICOS$^+$CD103$^+$ Treg cells.

MLL3 is frequently altered in human cancer, and emerging evidence has suggested its role in tumor suppression. However, how MLL3 and co-occurring cancer mutations control tumorigenesis has not been fully explored. In addition, the mechanisms by which MLL3 regulates cancer pathogenesis remained elusive. Using MaSC-based tumor models, we showed that loss of MLL3 dramatically accelerated tumor onset and growth by MaSCs with PI3K activation and p53 knockout mutations, a genetic setting that already induces rapid development of aggressive tumors [32], indicating a potent tumor suppressor role of MLL3 acting cooperatively with PI3K and p53 mutations. Furthermore, we revealed that loss of MLL3 led to the upregulation of HIF1α, which promoted both tumor cell-intrinsic stem cell activity and the cell-extrinsic effect on the recruitment of Foxp3$^+$ Treg cells. HIF1α expression correlates with poor clinical prognosis in many cancer types and contributes to a multitude of aggressive cancer behaviors, including proliferation, angiogenesis, metabolism, epithelial-mesenchymal transition, invasion, and cancer stemness [45,46]. Thus, our findings established a major role of MLL3 in mammary tumorigenesis and uncovered a mechanistic link between MLL3 and a key cancer signaling pathway.

HIFα (HIF1α and HIF2α) is often activated by the hypoxic tumor microenvironment in cancer, as 50 to 60% of solid tumors contain regions of hypoxia [47]. Interestingly, HIFα can also be regulated by mechanisms other than oxygen tension, and recent studies show that certain cancer stem cells exhibit high HIFα activity even under normoxia conditions [48,49]. How HIFα is regulated by hypoxia-independent mechanisms remains to be further elucidated. Here we found that MLL3 deletion led to the upregulation of HIF1α in the pre-onset tumor nodules, as well as elevated expression of HIF target genes in MaSC culture under normoxia. Interestingly, in large mammary tumors, HIF1α was robustly expressed regardless of MLL3 status. The pre-onset tumor nodules were embedded in the well-oxygenated normal mammary tissue, therefore likely non-hypoxic, whereas the large tumors are often hypoxic. It is likely that, in the non-hypoxic pre-onset nodules, MLL3 loss upregulated HIF1α in a hypoxia-independent manner. However, in the large tumors, hypoxia was sufficient to induce robust HIF1α expression, bypassing the effect of MLL3 deletion. Agreeing with this, MLL3 deletion increased Treg cell infiltration in pre-onset nodules, but not in large tumors. The precise biochemical mechanism by which MLL3 regulates HIF1α still needs to be determined. Recent studies have shown that HIF1α can be methylated in several lysine residues by histone lysine methyltransferases SET7/9 and G9a, and these modifications affect the stability or transcriptional activity of HIF1α [50-53]. Future studies are needed to determine whether MLL3 regulates HIF1α through similar mechanisms.

In breast cancer, HIF1α activation in hypoxic tumor cells can upregulate either the expression of the pluripotency transcription factor NANOG or the YAP/TAZ pathway to increase cancer stem cell frequency [45]. In contrast to this better understood cell-intrinsic role of HIF, the contribution of HIF to Treg cell recruitment appears to be context-dependent and requires further investigations [54]. We demonstrated a role of HIF1α-induced CCL2 in Treg recruitment in the very early stages of tumor onset. HIF1α binds to the genomic regions containing canonical HRE motifs near the *Ccl2* transcription start site, suggesting HIF1α directly activates *Ccl2* transcription. By activating the HIF1α-CCL2 pathway, MLL3 loss facilitates the establishment of an immunosuppressive microenvironment in early tumor lesions that are not yet hypoxic.

While the importance of the CCR2/CCL2 axis in cancer biology and beyond is well established and holds potentially important therapeutic promises [55], the complexity of associated mechanisms requires much further investigation. CCL2 produced by tumor cells and the stroma, mediates $CCR2^{+}Ly6C^{+}$ inflammatory monocytes recruitment, which enhances tumor growth and metastasis through various mechanisms such as secretion of the vascular endothelial growth factor (VEGF) and IL-6 [56,57]. Our high dimensional flow cytometry analysis of *Mll3*-mutant compared to MLL3 WT pre-onset tumor nodules revealed diverse subsets of $CD11b^{+}$ myeloid cells that include $CCR2^{+}$ monocytes and tumor associated $F4/80^{+}$ macrophages. However, we did not find any differences in their numbers whether the tumor cells expressed MLL3 or not, suggesting that the faster onset of *Mll3*-mutant tumors is unlikely to be related to a more competitive infiltration of these myeloid cells.

Interestingly, however, among the lymphocytes, Treg cells readily accumulated in greater numbers in MP5 compared to P5 pre-onset nodules. CCL2 from tumor cells was reported to attract $CCR2^{+}$ Treg cells from the dLNs to tumors in the MMTV-PyMT model of breast cancer [58]. Similarly, CCR2 can contribute to Treg cell recruitment to dLNs from inflamed tissues to suppress allograft rejection [59]. Consistent with such mechanism, we found that *Mll3*-mutant MaSCs secreted higher levels of CCL2, contributing to CCR2-mediated recruitment of Treg cells, likely from the tumor dLNs. While non-Treg $CD4^{+}$ T cells may still migrate to the *Mll3*-mutant pre-onset tumor nodules via CCR2 and convert to Treg cells, the fact that the proportion of non-Treg cells was comparable in both dLNs and pre-onset tumor nodules, but that this ratio became inverted only for Treg cells, rather suggested a direct recruitment of $CCR2^{+}$ Treg cells from the dLNs to the pre-onset tumor nodules. It is also likely that other chemotactic mechanisms are implicated since $CCR2^{-/-}$ Treg cells still infiltrated MP5 tumor nodules, albeit less efficiently than $CCR2^{+/+}$ cells. Treg cells were reported to migrate in response to CCR4/CCL22 and accumulate in breast and ovarian carcinoma tumors, which was associated with worse clinical outcomes and relapse in patients [60,61]. Likewise, expression of Foxp3 transcripts correlated with that of CCR4/CCL22 in the TCGA tumor data set for colon, breast, pancreas and lung cancers [62]. Transcriptomic analysis of tumor-infiltrating human Treg cells in breast cancer compared to normal breast tissue-resident Treg cells, showed an increased expression of genes encoding for multiple chemotactic receptors (CCR5, CCR8, CCR10, CXCR3, CX3CR1, CXCR6), which was also associated with more aggressive cancers [63].

In contrast to the tumor-infiltrating Treg cells, dLN Treg cells neither expressed KLRG1 nor ICOS or CD103, suggesting that Treg cells newly recruited to pre-onset tumors further

differentiated into activated, proliferative Treg cells in this microenvironment. Tumor-infiltrating Treg cells were reported to be more suppressive and to exhibit an activated proliferative ($Ki67^+$) phenotype [60,63], consistent with our results. MP5 pre-onset tumor nodules contained an expanded population of Treg cells that included a significant proportion of $KLRG1^+$ proliferative ($Ki67^+$) Treg cells. $KLRG1^+$ Treg cells were described as an antigen-specific, terminally differentiated proliferative and short-lived subset preferentially residing in mucosal tissues -notably the gut lamina propria-, and which development required extensive IL-2 signaling [34] and/or Treg cell homeostatic proliferation [64]. *Mll3*-mutant pre-onset tumor-infiltrating $KLRG1^+$ Treg cells are $CD62L^{low}$, $CD44^{hi}$, $CD103^{hi}$, $Ki67^{hi}$, in line with the previously reported phenotype, and the possibility that they recognize and proliferate in response to tumor-derived antigens..

Besides its powerful and well-established chemotactic function, CCL2 can directly signal to CCR2 to activate multiple pathways (PI3K/Akt, RAC GTPase, PKC, JAK/STAT) and subsequent biological responses [55]. Lack of CCR2 on T cells promoted accumulation of Treg cells in spite of Th17 T cells in a model of colitis [65]. Contrasting with this report, CCR2 deficiency can also result in a loss of Treg cells as a consequence of the loss of Treg cell fitness [66]. While these data are conflicting, it is nevertheless a proof of concept that CCR2 signaling, independent of its chemotactic role, could act as a key signal orchestrating Treg cell differentiation in our early-stage pre-onset breast tumors.

In summary, our work demonstrates a major role of MLL3 loss in driving mammary tumor onset and growth through regulating tumor cell-intrinsic stem cell activity and establishing an immunosuppressive microenvironment via Treg cell recruitment. We link MLL3 loss, HIF1α activation, and CCL2 secretion, which reveals an important cancer signaling pathway mediating MLL3 functions. Additionally, as CCL2 is an essential chemokine for the recruitment of multiple types of pro-tumor immune cells [55], the HIF1α-CCL2 pathway is therefore likely to have a broad role in regulating tumor immune microenvironment in hypoxic tumors.

EXPERIMENTAL PROCEDURES

Ethics statement

This study was carried out in strict accordance with the approvals by the animal use committee at the Albert Einstein College of Medicine. All efforts were made to minimize suffering and provide humane treatment to the animals included in the study.

Mice

All mice were bred in the SPF animal facility at the Albert Einstein College of Medicine. Wild-type (WT) C57BL/6J (B6) (JAX, #000664), FVB/n (JAX, #001800), Pik3ca* (JAX, #012343), Pik3ca^{H1047R} (JAX, #016977), *Rag1*$^{-/-}$ (JAX, #002216) and *Ccr2*^{KO} (JAX, #004999) mice were purchased from the Jackson Laboratory.

MaSC organoid culture

Organoid medium was prepared with Advanced DMEM/F-12 (Life Technologies) supplemented with 5% heat-inactivated FBS (Sigma, F2442), 10 ng/ml EGF (Sigma, E9644), 20 ng/ml FGF2 (EMD Millipore, GF003), 4 μg/ml heparin (Sigma, H3149), 5 μM Y-27632 (Cayman Chemical, #10005583) and 5% Matrigel (Corning, #354234). For passaging and expansion, organoids were washed with PBS, dissociated with 0.05% trypsin/EDTA and seeded at 3×10^5 cells/well in 6-well ultra-low attachment plates. Cells were then passaged every 3-4 days. Dissociated organoid cells were frozen in calf serum containing 10% DMSO and 5 μM Y-27632, and thawed to reestablish the culture. For all organoid formation and proliferation assays, 500 cells/well were seeded in 96-well ultra-low attachment plates (Corning). For quantifying organoid-forming efficiency, the number of organoids (≥ 100 μm in diameter) was counted 3-4 days after seeding, subsequently organoids were dissociated as described above and counted for cell number. For hypoxia experiments, organoids were cultured for 24 hrs or 3 days at 1% O_2.

Isolating MaSCs and Tumor Cell lines

Mammary glands or Tumors ~100mm^3 were minced and digested with 300 units/ml collagenase type 3 (Worthington Biochemical, LS004182), and 10 μg/ml DNase I (Worthington Biochemical, LS002139) in the DMEM/F-12 medium at 37°C for 2 hrs on an orbital shaker (100 units/ml hyaluronidase added only for tumor digestion). The digested samples were washed with PBS and were further digested with 0.05% trypsin-EDTA for 5 minutes and 1 unit/ml neutral protease (dispase) (Worthington Biochemical, LS02109) plus 100 ug/ml DNase (Roche) for 5 minutes. The digested cells were then filtered through 40 μm cell strainers to obtain single cells. All experiments were done at passage 8-15 for MaSC lines and passage 0-1 for tumor cell lines.

Viral transduction

Lentiviruses were produced with the pMD2.G and pCMVR8.74 packaging system, a gift from Didier Trono (Addgene, plasmids #12259 and #22036). Viruses were concentrated with the Lenti-X Concentrator reagent (Clontech, #631232). For viral transduction, dissociated organoid cells were seeded in virus-containing organoid culture media with 5 μg/ml polybrene (EMD-Millipore TR-1003-G) overnight, and medium was refreshed the next day. Transduced cells were either FACS sorted by GFP or RFP (70-90% transduction efficiency) or selected by puromycin treatment (2 μg/ml).

CRISPR-based genome editing

Genome editing for Pik3ca^{H1047R} MaSCs (FVB/n background) were carried out as following: MaSCs (passage 2-3) were transduced with sgP53 or sgNT cloned into lentiCRISPRv2-puro (Addgene, Plasmid #98290), passaged once, and then transduced with sgMll3 or sgNT cloned into pLKO5.sgRNA.EFS.tRFP (Addgene, plasmid #57823). Cells were grown for 3 days and selected with puromycin for 3 days. Next, cells were infected with Adeno-Cre-GFP and sorted for GFP/RFP double positive cells. MP5-Hif1α KO lines were made via transducing MP5 cells with sgHif1a or sgNT cloned into lentiCRISPRv2-GFP (Addgene, plasmid #82416) and sorting for GFP.

Genome editing for Pik3ca* MaSCs (B6 background) were carried out as following: MaSCs (passage 2) were transduced with sgP53 or sgNT cloned into lentiCRISPRv2-puro, passaged once and infected with Ad-Cre-GFP, and puromycin selected for 3 days. Cells were then transduced with sgMll3 or sgNT cloned into pLKO5.sgRNA.EFS.tRFP and sorted for GFP/RFP double positive cells.

Targeting sequences for sgRNAs are as following: sgMll3 GCACACGATCTAGTACTCAG (Exon10), sgp53 CCTCGAGCTCCCTCTGAGCC (Exon 2), sgNT GCGAGGTATTCGGCTCCGCG, and sgHif1a CACAATGTGAGCTCACATCT (Exon 2).

Tumor onset and growth

Organoids were cultured for 3-4 days, then dissociated and passed through 40µm cell strainer to obtain single cells. Single cells (3 x 10^5) suspended in PBS and 25% Matrigel were orthotopically injected per #3 mammary gland of B6 or FVB WT mice aged 6-8 weeks. Specifically, P5 and MP5 lines #1, #3, #4 and Hif1a-KO lines were transplanted to FVB mice and lines #2 and #7 were transplanted to mouse models of B6 background. Tumor onset was monitored by weekly palpation, and Kaplan-Meier survival analysis was used to compare tumor onset. Tumor onset was scored when at least one dimension of the tumor measured ≥3mm. Tumor volume was measured by caliper and calculated as $V = 0.532 \times Length \times Width^2$. All experiments done on pre-onset nodules (≤ 3mm or 20mm^3) were extracted on 20 days for P5 and 10 days for MP5 post transplantation due to the ~2-fold difference in growth rate between these two tumor types.

Immunofluorescence tissue sections and western blot

Formalin-fixed paraffin-embedded sections for organoids or tumors were stained with antibodies against HIF1α, Ki67, Foxp3, H3K4me1, H3K4me2, and H3K27ac. Western blots were performed with antibodies against mouse MLL3, Phospho-Akt (Ser473), HIF1α, H3K4me1, H3K4me2, H3K27ac , Histone H3, β-actin, and α-tubulin (see Table S1 for antibody sources and dilutions).

Preparation of cell suspensions for flow cytometry and adoptive transfers

Tumors were minced into 2-4 mm fragments, which were incubated in HBSS medium with 10 UI/mL collagenase I, 400 UI/mL collagenase D and 30 µg/mL at 37°C for 1 hr under agitation. After, the fragments were homogenized, filtered through a 100µm nylon mesh cell strainer and cells were centrifuged at 1,450 rpm for 10 min at 4°C. Draining lymph nodes were incubated in HBSS medium with 400 UI/mL collagenase D at 37°C for 1 hr under agitation. BM cells were obtained by flushing femur with complete medium (RPMI 1640, 10% FBS, 1% Penicillin/Streptomycin, 55µM β-mercaptoethanol, 1mM Sodium Pyruvate, 1X Glutamax, 1X non-essential amino acids) containing 10% FCS.

Cell-staining for FACS analysis
Cell suspensions were incubated with 2.4G2 Fc Block Ab and stained in PBS 1%FCS, 2mM EDTA, 0.02% sodium azide with fluorescently tagged Abs purchased from eBioscience, BD Biosciences, R&D systems, or BioLegend (See Tables S1). Brilliant stain buffer (BD) was used when more than two Abs were conjugated with BD Horizon Brilliant fluorescent polymer dyes. Cells were stained for cell-surface marker expression, then fixed in eBioscience Fixation/Permeabilization buffer prior to intracellular granzyme B and Foxp3 transcription factor (TF) staining in eBioscience Permeabilization buffer for 1hr. Data acquisition was done using a FACSAria III or a Cytek Aurora flow cytometer. All flow cytometry data were analyzed using FlowJo v9 or v10 software (TreeStar).

ChIP-qPCR
After one day of 5% O_2 hypoxia culture, MP5 line#3 cells were crosslinked with 1% formaldehyde at room temperature based on ENCODE protocol [67]. Crosslinked cells were subjected to the sonication process with Bioruptor (30 sec ON/30 sec OFF, 60 cycles, High speed), and the fragmentation was validated by electrophoresis in a 1% agarose gel. 30 µg chromatin was used for each immunoprecipitation (IP) and 5 µg chromatin was used for input. Briefly, 200 µL of Dynabeads M-280 Sheep Anti-Mouse IgG (Invitrogen, #11201D) washed with wash buffer (5 mg/mL BSA in PBS) was mixed with 1 µg Hif1a Ab (Novus Biologicals, NB-100-105) for 4 hrs at 4°C rotating. After washing antibody-bound beads in 100 mM Tris-HCl pH 7.5, 500 mM LiCl, 1% NP-40, 1% sodium deoxycholate, the beads were resuspended with fractionated chromatin by magnetic stand, mixed for 1 hrs at room temperature, then 3 hrs at 4°C rotating. The chromatin conjugated beads were further washed with LiCl IP wash buffer for 4 times, following wash with TE buffer (10 mM Tris-HCl pH 7.5, 0.1 M Na2EDTA). The washed chromatin conjugated beads were incubated at 65℃ overnight to reverse crosslink. ChIP DNA and Input DNA were purified with ChIP DNA Clean & Concentrator (Zymo Research, #D5205). Quantitative PCR was performed with PowerUp SYBR Green Master Mix (ThermoFisher, #A25742), according to the protocol provided with the kit. See Table S2 for primer sequences.

Multiplex-beads array assay
A custom-made mouse Cytokine 26-Plex-assay kit was designed and purchased from Invitrogen. The kit included specific quantification of mouse Eotaxin, IL-1α, IL-1β, IL-2, IL-3, IL-4, IL-5, IL6, IL-7, IL-9, IL-10, IL-12p70, IL-13, IL-15/IL-15R, IL25, CCL2, CCL3, CCL4, CCL5, CXCL2, CXCL10, TNFα, IFN-γ, GM-CSF, VEGF, GM-CSF, MCSF. Lyophilized standards were reconstituted with kit Assay Diluent and combined to 1 mL for stock solution and serially diluted to generate standard curves for each cytokine. Samples were diluted with Assay Diluent and the assay was performed in a 96-well filter plate using the kit's components, according to the manufacturer's protocol.

Generation of bone-marrow chimera mice
Lethally irradiated (1,200 rads) WT B6 female mice were immediately reconstituted with a total of 2×10^6 BM cells isolated from C*cr2*^{KO} and WT at a 1:1 ratio. Chimerism of reconstituted mice was checked ~6-8 weeks later in the blood, prior to MaSCs injection.

***In vivo* anti-CCL2 or isotype Ab treatment**

Anti-mouse MCP-1/CCL2 (clone 2H5) and hamster IgG2a isotype-control were purchased from BioXCell (USA). 3 days post MaSCs injection, treatment with anti-CCL2 or isotype Ab at 1mg/kg was initiated and repeated every 3 days across the course of the experiment.

Statistical analysis

P values were calculated using unpaired t-test except when otherwise specified. All analyses were done in GraphPad Prism 9. $P < 0.05$ was considered significant.

Acknowledgments: We thank the Einstein FACS, Histopathology, Analytical Imaging, and Stem Cell Isolation core facilities.

Funding: This work was funded by the Department of Defense Breakthrough awards BC161696 and BC200410 to GL and WG, Hirschl Caulier Award to GL, and the NIH grant 1R01CA212424 and the Mary Kay Foundation grant 04-19 to WG. MB received fellowships from Fondation pour le Recherche Medicale. NC and EG are respectively supported by NIH Supplement to AI103338 (NC) and NIH R25 GM104547 (EG) and MSTP training grant T32 GM7288 (EG). Core resources for Einstein core facilities were supported by the Einstein Cancer Center (NCI cancer center support grant 2P30CA013330) and the NYSTEM shared facility grant support (C029154).

Author contribution: MB and PE designed, performed and interpreted a majority of experiments, assembled all Figures, and contributed to writing/editing of the manuscript. KN, with the guidance of MS, conducted and interpreted the ChIP experiments, and contributed to writing/editing of the manuscript. EG conducted and analyzed the Luminex assays. NC set up the high-dimensional FACS panels. ZZ developed and analyzed the initial P5/MP5 tumor models. GL and WG designed and interpreted experiments with all authors, contributed to Figure design and editing, and wrote the paper.

Competing interests: The authors declare that no competing interests exist.

Data materials and availability: All data is available in the main text or the supplementary materials.

REFERENCES

1. O'Donnell, J.S., Teng, M.W.L. & Smyth, M.J. Cancer immunoediting and resistance to T cell-based immunotherapy. *Nat Rev Clin Oncol* **16**, 151-167 (2019).
2. Dunn, G.P., Old, L.J. & Schreiber, R.D. The three Es of cancer immunoediting. *Annu Rev Immunol* **22**, 329-360 (2004).
3. Noman, M.Z*., et al.* PD-L1 is a novel direct target of HIF-1alpha, and its blockade under hypoxia enhanced MDSC-mediated T cell activation. *J Exp Med* **211**, 781-790 (2014).
4. Loke, P. & Allison, J.P. PD-L1 and PD-L2 are differentially regulated by Th1 and Th2 cells. *Proc Natl Acad Sci U S A* **100**, 5336-5341 (2003).
5. Shurin, M.R*., et al.* Intratumoral cytokines/chemokines/growth factors and tumor infiltrating dendritic cells: friends or enemies? *Cancer Metastasis Rev* **25**, 333-356 (2006).
6. Chanmee, T., Ontong, P., Konno, K. & Itano, N. Tumor-associated macrophages as major players in the tumor microenvironment. *Cancers (Basel)* **6**, 1670-1690 (2014).
7. Kumar, V., Patel, S., Tcyganov, E. & Gabrilovich, D.I. The Nature of Myeloid-Derived Suppressor Cells in the Tumor Microenvironment. *Trends Immunol* **37**, 208-220 (2016).
8. Youn, J.I., Nagaraj, S., Collazo, M. & Gabrilovich, D.I. Subsets of myeloid-derived suppressor cells in tumor-bearing mice. *J Immunol* **181**, 5791-5802 (2008).
9. Munoz-Fontela, C., Mandinova, A., Aaronson, S.A. & Lee, S.W. Emerging roles of p53 and other tumour-suppressor genes in immune regulation. *Nat Rev Immunol* **16**, 741-750 (2016).
10. Casey, S.C*., et al.* MYC regulates the antitumor immune response through CD47 and PD-L1. *Science* **352**, 227-231 (2016).
11. Textor, S*., et al.* Human NK cells are alerted to induction of p53 in cancer cells by upregulation of the NKG2D ligands ULBP1 and ULBP2. *Cancer Res* **71**, 5998-6009 (2011).
12. Iannello, A., Thompson, T.W., Ardolino, M., Lowe, S.W. & Raulet, D.H. p53-dependent chemokine production by senescent tumor cells supports NKG2D-dependent tumor elimination by natural killer cells. *J Exp Med* **210**, 2057-2069 (2013).
13. Santhanam, U., Ray, A. & Sehgal, P.B. Repression of the interleukin 6 gene promoter by p53 and the retinoblastoma susceptibility gene product. *Proc Natl Acad Sci U S A* **88**, 7605-7609 (1991).
14. Spranger, S., Bao, R. & Gajewski, T.F. Melanoma-intrinsic beta-catenin signalling prevents anti-tumour immunity. *Nature* **523**, 231-235 (2015).
15. Peng, W*., et al.* Loss of PTEN Promotes Resistance to T Cell-Mediated Immunotherapy. *Cancer Discov* **6**, 202-216 (2016).
16. Torre, L.A*., et al.* Global cancer statistics, 2012. *CA: a cancer journal for clinicians* **65**, 87-108 (2015).
17. Howlader, N*., et al.* SEER Cancer Statistics Review, 1975-2018. *National Cancer Institute, Bethesda, MD*, https://seer.cancer.gov/csr/1975_2018/ (2020).
18. Sze, C.C. & Shilatifard, A. MLL3/MLL4/COMPASS Family on Epigenetic Regulation of Enhancer Function and Cancer. *Cold Spring Harbor perspectives in medicine* **6**(2016).
19. Lawrence, M.S*., et al.* Discovery and saturation analysis of cancer genes across 21 tumour types. *Nature* **505**, 495-501 (2014).
20. Ding, L*., et al.* Perspective on Oncogenic Processes at the End of the Beginning of Cancer Genomics. *Cell* **173**, 305-320.e310 (2018).
21. TCGA Network. Comprehensive molecular portraits of human breast tumours. *Nature* **490**, 61-70 (2012).

22. Ciriello, G.*, et al.* Comprehensive Molecular Portraits of Invasive Lobular Breast Cancer. *Cell* **163**, 506-519 (2015).
23. Razavi, P.*, et al.* The Genomic Landscape of Endocrine-Resistant Advanced Breast Cancers. *Cancer Cell* **34**, 427-438.e426 (2018).
24. Lee, J.*, et al.* A tumor suppressive coactivator complex of p53 containing ASC-2 and histone H3-lysine-4 methyltransferase MLL3 or its paralogue MLL4. *Proc Natl Acad Sci U S A* **106**, 8513-8518 (2009).
25. Chen, C.*, et al.* MLL3 Is a Haploinsufficient 7q Tumor Suppressor in Acute Myeloid Leukemia. *Cancer Cell* **25**, 652-665 (2014).
26. Wang, L.*, et al.* Resetting the epigenetic balance of Polycomb and COMPASS function at enhancers for cancer therapy. *Nat Med* **24**, 758-769 (2018).
27. Zhang, Z.*, et al.* Mammary-Stem-Cell-Based Somatic Mouse Models Reveal Breast Cancer Drivers Causing Cell Fate Dysregulation. *Cell reports* **16**, 3146-3156 (2016).
28. Jozwik, K.M., Chernukhin, I., Serandour, A.A., Nagarajan, S. & Carroll, J.S. FOXA1 Directs H3K4 Monomethylation at Enhancers via Recruitment of the Methyltransferase MLL3. *Cell reports* **17**, 2715-2723 (2016).
29. Gala, K.*, et al.* KMT2C mediates the estrogen dependence of breast cancer through regulation of ERalpha enhancer function. *Oncogene* **37**, 4692-4710 (2018).
30. Zehir, A.*, et al.* Mutational landscape of metastatic cancer revealed from prospective clinical sequencing of 10,000 patients. *Nat Med* **23**, 703-713 (2017).
31. Perou, C.M. & Borresen-Dale, A.L. Systems biology and genomics of breast cancer. *Cold Spring Harb Perspect Biol* **3**, doi: 10.1101/cshperspect.a003293 (2011).
32. Adams, J.R.*, et al.* Cooperation between Pik3ca and p53 mutations in mouse mammary tumor formation. *Cancer Res* **71**, 2706-2717 (2011).
33. Srinivasan, L.*, et al.* PI3 kinase signals BCR-dependent mature B cell survival. *Cell* **139**, 573-586 (2009).
34. Cheng, G.*, et al.* IL-2 receptor signaling is essential for the development of Klrg1+ terminally differentiated T regulatory cells. *J Immunol* **189**, 1780-1791 (2012).
35. Panduro, M., Benoist, C. & Mathis, D. Tissue Tregs. *Annu Rev Immunol* **34**, 609-633 (2016).
36. Stephens, G.L., Andersson, J. & Shevach, E.M. Distinct subsets of FoxP3+ regulatory T cells participate in the control of immune responses. *J Immunol* **178**, 6901-6911 (2007).
37. Mami-Chouaib, F.*, et al.* Resident memory T cells, critical components in tumor immunology. *J Immunother Cancer* **6**, 87 (2018).
38. Chandrasekaran, S. & King, M.R. Microenvironment of tumor-draining lymph nodes: opportunities for liposome-based targeted therapy. *Int J Mol Sci* **15**, 20209-20239 (2014).
39. Guo, W.*, et al.* Slug and Sox9 cooperatively determine the mammary stem cell state. *Cell* **148**, 1015-1028 (2012).
40. Chen, X.*, et al.* XBP1 promotes triple-negative breast cancer by controlling the HIF1alpha pathway. *Nature* **508**, 103-107 (2014).
41. Briggs, K.J.*, et al.* Paracrine Induction of HIF by Glutamate in Breast Cancer: EglN1 Senses Cysteine. *Cell* **166**, 126-139 (2016).
42. Wu, M.Z.*, et al.* Hypoxia Drives Breast Tumor Malignancy through a TET-TNFalpha-p38-MAPK Signaling Axis. *Cancer Res* **75**, 3912-3924 (2015).
43. Singha, B., Gatla, H.R. & Vancurova, I. Transcriptional regulation of chemokine expression in ovarian cancer. *Biomolecules* **5**, 223-243 (2015).

44. Nakatsumi, H., Matsumoto, M. & Nakayama, K.I. Noncanonical Pathway for Regulation of CCL2 Expression by an mTORC1-FOXK1 Axis Promotes Recruitment of Tumor-Associated Macrophages. *Cell reports* **21**, 2471-2486 (2017).
45. Schito, L. & Semenza, G.L. Hypoxia-Inducible Factors: Master Regulators of Cancer Progression. *Trends Cancer* **2**, 758-770 (2016).
46. Keith, B., Johnson, R.S. & Simon, M.C. HIF1α and HIF2α: sibling rivalry in hypoxic tumour growth and progression. *Nat Rev Cancer* **12**, 9-22 (2011).
47. Rankin, E.B. & Giaccia, A.J. Hypoxic control of metastasis. *Science* **352**, 175-180 (2016).
48. Lee, K.M.*, et al.* MYC and MCL1 Cooperatively Promote Chemotherapy-Resistant Breast Cancer Stem Cells via Regulation of Mitochondrial Oxidative Phosphorylation. *Cell metabolism* **26**, 633-647 e637 (2017).
49. Wang, Y., Liu, Y., Malek, S.N., Zheng, P. & Liu, Y. Targeting HIF1α eliminates cancer stem cells in hematological malignancies. *Cell Stem Cell* **8**, 399-411 (2011).
50. Liu, X.*, et al.* Repression of hypoxia-inducible factor alpha signaling by Set7-mediated methylation. *Nucleic Acids Res* **43**, 5081-5098 (2015).
51. Kim, Y.*, et al.* Methylation-dependent regulation of HIF-1alpha stability restricts retinal and tumour angiogenesis. *Nat Commun* **7**, 10347 (2016).
52. Liu, Q., Geng, H., Xue, C., Beer, T.M. & Qian, D.Z. Functional regulation of hypoxia inducible factor-1alpha by SET9 lysine methyltransferase. *Biochimica et biophysica acta* **1853**, 881-891 (2015).
53. Bao, L.*, et al.* Methylation of hypoxia-inducible factor (HIF)-1α by G9a/GLP inhibits HIF-1 transcriptional activity and cell migration. *Nucleic Acids Res* **46**, 6576-6591 (2018).
54. Palazon, A., Goldrath, A.W., Nizet, V. & Johnson, R.S. HIF transcription factors, inflammation, and immunity. *Immunity* **41**, 518-528 (2014).
55. Fei, L., Ren, X., Yu, H. & Zhan, Y. Targeting the CCL2/CCR2 Axis in Cancer Immunotherapy: One Stone, Three Birds? *Front Immunol* **12**, 771210 (2021).
56. Qian, B.Z.*, et al.* CCL2 recruits inflammatory monocytes to facilitate breast-tumour metastasis. *Nature* **475**, 222-225 (2011).
57. Bonapace, L.*, et al.* Cessation of CCL2 inhibition accelerates breast cancer metastasis by promoting angiogenesis. *Nature* **515**, 130-133 (2014).
58. Loyher, P.L.*, et al.* CCR2 Influences T Regulatory Cell Migration to Tumors and Serves as a Biomarker of Cyclophosphamide Sensitivity. *Cancer Res* **76**, 6483-6494 (2016).
59. Zhang, N.*, et al.* Regulatory T cells sequentially migrate from inflamed tissues to draining lymph nodes to suppress the alloimmune response. *Immunity* **30**, 458-469 (2009).
60. Curiel, T.J.*, et al.* Specific recruitment of regulatory T cells in ovarian carcinoma fosters immune privilege and predicts reduced survival. *Nat Med* **10**, 942-949 (2004).
61. Gobert, M.*, et al.* Regulatory T cells recruited through CCL22/CCR4 are selectively activated in lymphoid infiltrates surrounding primary breast tumors and lead to an adverse clinical outcome. *Cancer Res* **69**, 2000-2009 (2009).
62. Magnuson, A.M.*, et al.* Identification and validation of a tumor-infiltrating Treg transcriptional signature conserved across species and tumor types. *Proc Natl Acad Sci U S A* **115**, E10672-E10681 (2018).
63. Plitas, G.*, et al.* Regulatory T Cells Exhibit Distinct Features in Human Breast Cancer. *Immunity* **45**, 1122-1134 (2016).
64. Feuerer, M.*, et al.* Genomic definition of multiple ex vivo regulatory T cell subphenotypes. *Proc Natl Acad Sci U S A* **107**, 5919-5924 (2010).

65. Bakos, E.*, et al.* CCR2 Regulates the Immune Response by Modulating the Interconversion and Function of Effector and Regulatory T Cells. *J Immunol* **198**, 4659-4671 (2017).
66. Zhan, Y.*, et al.* CCR2 enhances CD25 expression by FoxP3(+) regulatory T cells and regulates their abundance independently of chemotaxis and CCR2(+) myeloid cells. *Cell Mol Immunol* **17**, 123-132 (2020).
67. Landt, S.G.*, et al.* ChIP-seq guidelines and practices of the ENCODE and modENCODE consortia. *Genome Res* **22**, 1813-1831 (2012).

FIGURES

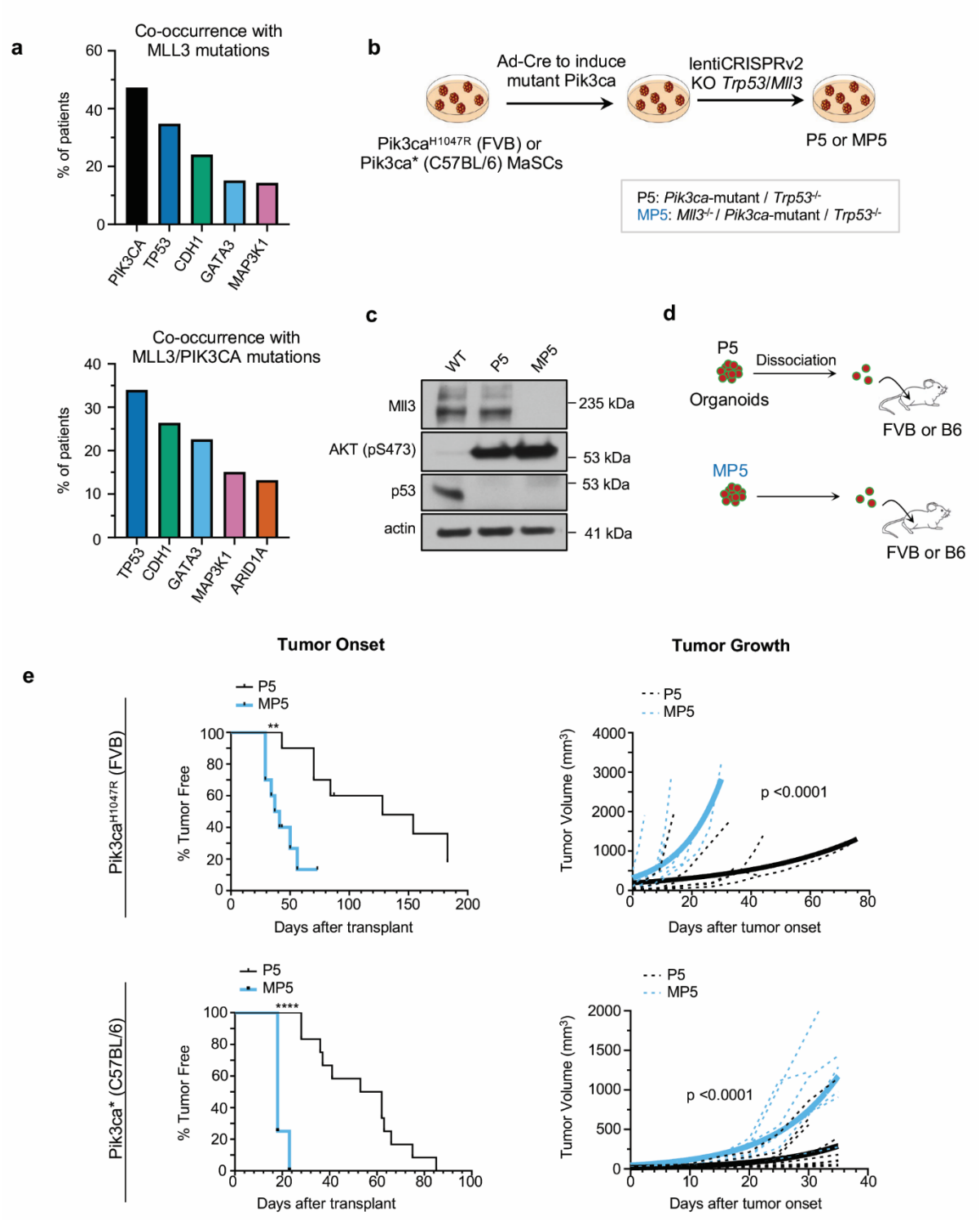

Figure 1. Loss of Mll3 cooperates with PIK3CA and p53 mutations to drive tumor initiation and growth. (a) MSKCC-IMPACT 2017 Breast Cancer database analysis of common mutations co-occurring in patients with MLL3 mutations (top) and with both MLL3/PIK3CA mutations

(bottom). **(b)** Generation of Pik3ca-mutant/p53$^{-/-}$ (P5) and Pik3ca-mutant/p53$^{-/-}$/Mll3$^{-/-}$ (MP5) mouse mammary stem cell organoids. **(c)** Western blot validation of Pik3ca activation mutation, Mll3 deletion, and p53 deletion in MaSC organoids. **(d)** Schematic of single cell MaSC transplantation to recipient mouse mammary fat pads of FVB or B6 WT mice. Organoids cultured for 3 days were dissociated into single cells, and $3x10^5$ cells injected per inguinal gland. **(e)** Kaplan-Meier survival analysis of tumor onset (left), and tumor growth rate analysis (right) for P5 tumors (n=10) compared to MP5 tumors (n=10) expressing Pik3ca^{H1047R} (line #1) (top) and P5 tumors (n=12) compared to MP5 tumors (n=8) expressing Pik3ca* (line #7) (bottom). P-values (**$p< 0.01$ and ****$p< 0.0001$) are indicated.

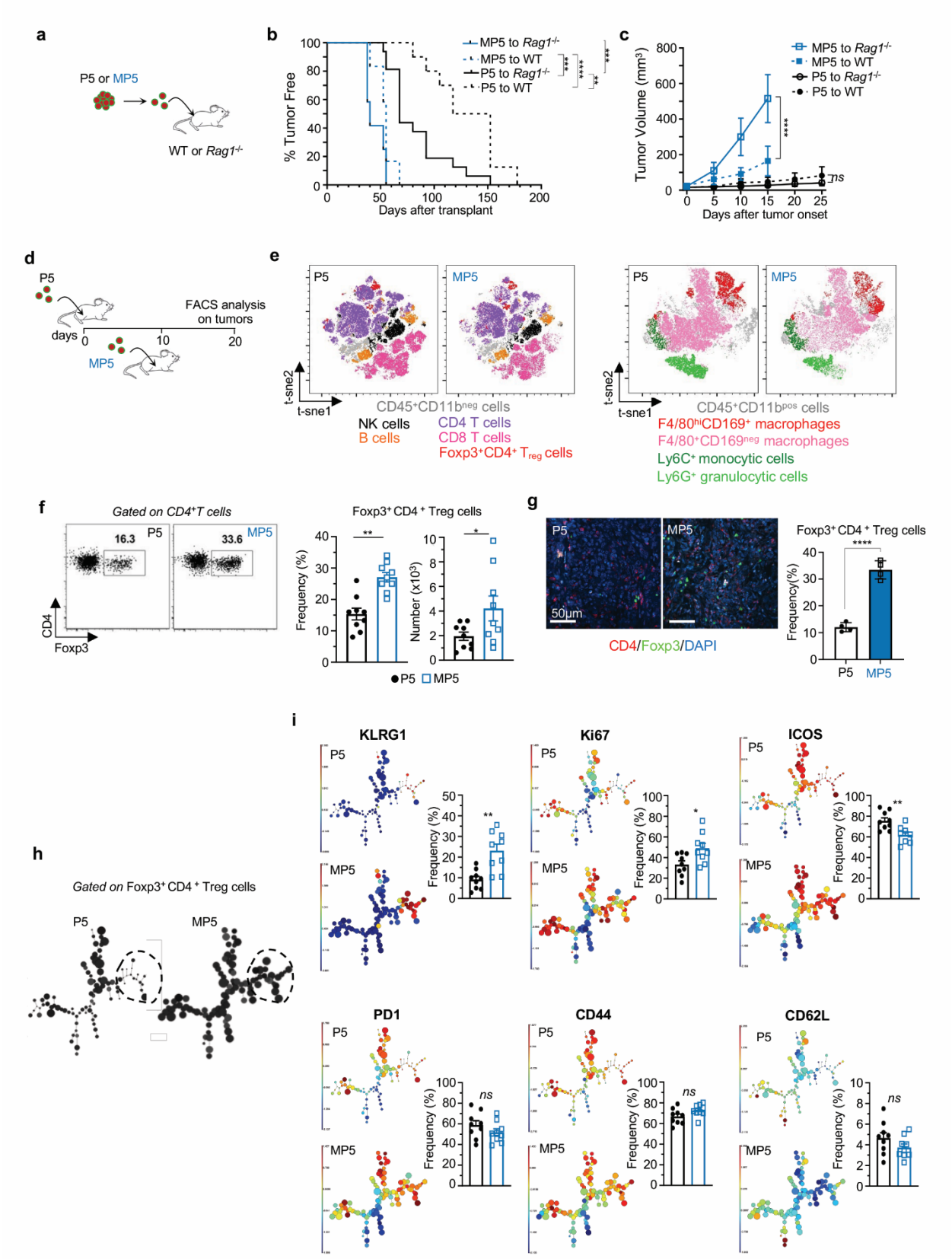
a
P5 or MP5
WT or Rag1-/-
b
% Tumor Free
Days after transplant
MP5 to Rag1-/-
MP5 to WT
P5 to Rag1-/-
P5 to WT
c
Tumor Volume (mm3)
Days after tumor onset
ns
d
P5
MP5
days
FACS analysis on tumors
e
P5
MP5
t-sne1
t-sne2
CD45+CD11bneg cells
NK cells
B cells
CD4 T cells
CD8 T cells
Foxp3+CD4+ Treg cells
CD45+CD11bpos cells
F4/80hiCD169+ macrophages
F4/80+CD169neg macrophages
Ly6C+ monocytic cells
Ly6G+ granulocytic cells
f
Gated on CD4+T cells
16.3
33.6
CD4
Foxp3
Foxp3+ CD4 + Treg cells
Frequency (%)
Number (x10³)
P5
MP5
g
50µm
CD4/Foxp3/DAPI
Frequency(%)
h
Gated on Foxp3+ CD4 + Treg cells
i
KLRG1
Ki67
ICOS
PD1
CD44
CD62L
Frequency (%)
ns

Figure 2. Loss of Mll3 promotes Treg cell infiltration during tumor initiation. (a) Schematics of transplant strategy as in Fig. 1d. P5 or MP5 MaSCs were transplanted into B6 WT or *Rag1*$^{-/-}$ mice, 3x10^5 single cells per number 4 mammary gland. **(b)** Kaplan-Meier survival analysis of tumor onset for P5 tumors compared to MP5 tumors from line #7 transplanted to WT B6 mice and *Rag1*$^{-/-}$ mice (n=10-16 tumors per group, pooled from two independent experiments). **(c)** Tumor growth rate of P5 compared to MP5 tumors from line #7 transplanted to WT B6 mice and *Rag1*$^{-/-}$ mice (n=10-16 tumors per group, pooled from two independent experiments). **(d)** Schematics of transplant strategy. P5 or MP5 MaSCs from line #3 were transplanted into FVB mice, 3x10^5 single cells per number 4 mammary gland. Pre-onset tumor nodules were extracted and analyzed by flow cytometry (20 and 10 days post-transplant, respectively). **(e)** Tumor samples were stained for immune cell lineages and analyzed by flow cytometry. T-SNE overlays of subsets of immune cells as defined by the color codes. Data represent 2 replicate experiments. **(f)** Graphs show the frequency and the number of CD4$^+$Foxp3$^+$ Treg cells with representative dot plots. Data (e, f) are from 3 independent replicate experiments (n=9, P5 and MP5 pre-onset tumor nodules from line #3). **(g)** Immunofluorescence images and quantification of CD4 and Foxp3 co-expression in sections of P5 compared to MP5 pre-onset tumor nodules at 20 and 10 days post-transplant, respectively (n=4, P5 and MP5 pre-onset tumor nodules from line #3). **(h)** FlowSOM unsupervised clustering of P5 and MP5 Foxp3$^+$CD4$^+$Treg cells across 9 pre-onset tumor nodules per group. Each node is proportional to cell numbers. **(i)** FlowSOM representation for indicated markers on Foxp3$^+$CD4$^+$Treg cells from P5 and MP5 pre-onset tumor nodules. Each node is proportional to cell numbers and color scale is proportional to mean fluorescence intensity of indicated markers. P-values (*< 0.05, **< 0.01, ***< 0.001 and ****< 0.0001) are indicated.

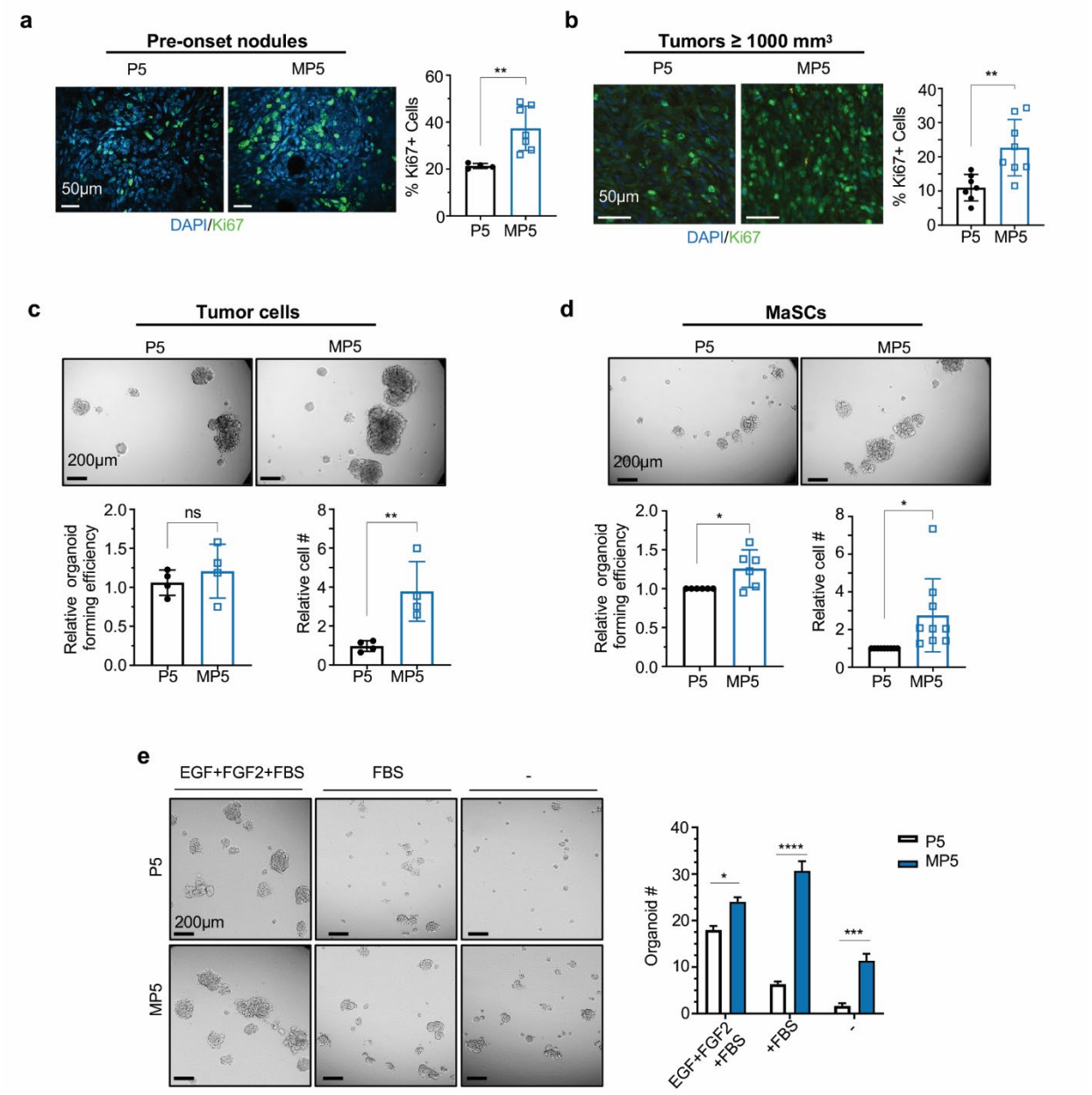

Figure 3. Loss of Mll3 promotes tumor cell-intrinsic proliferative and organoid forming potential. (a) Immunofluorescence images and quantification of Ki67 expression in P5 pre-onset tumor nodules (n=4) compared to matched MP5 pre-onset tumor nodules (n=7) from line #3. **(b)** Immunofluorescence images and quantification of Ki67 expression in P5 tumors (n=7) compared to MP5 tumors (n=8) (combined data from lines #1 and #3; tumors larger than 1000mm^3). **(c)** Relative organoid-forming efficiency and cell growth of MP5 (n=4) compared to P5 (n=4) tumor cells (freshly isolated from individual tumors transplanted from line #3) in full organoid medium. **(d)** Relative organoid-forming efficiency and cell number for matched pairs of MP5 versus P5 MaSC organoids in full organoid medium: Line #1, #2, #3, #4, and #7. Each line normalized to its matched P5 control. **(e)** Organoid-forming efficiency of P5 compared to MP5 MaSC line #7 in full

organoid medium, no growth factor medium and no growth factor and serum medium. P-values (*p< 0.05, **p< 0.01, ***p< 0.001 and ****p< 0.0001) are indicated.

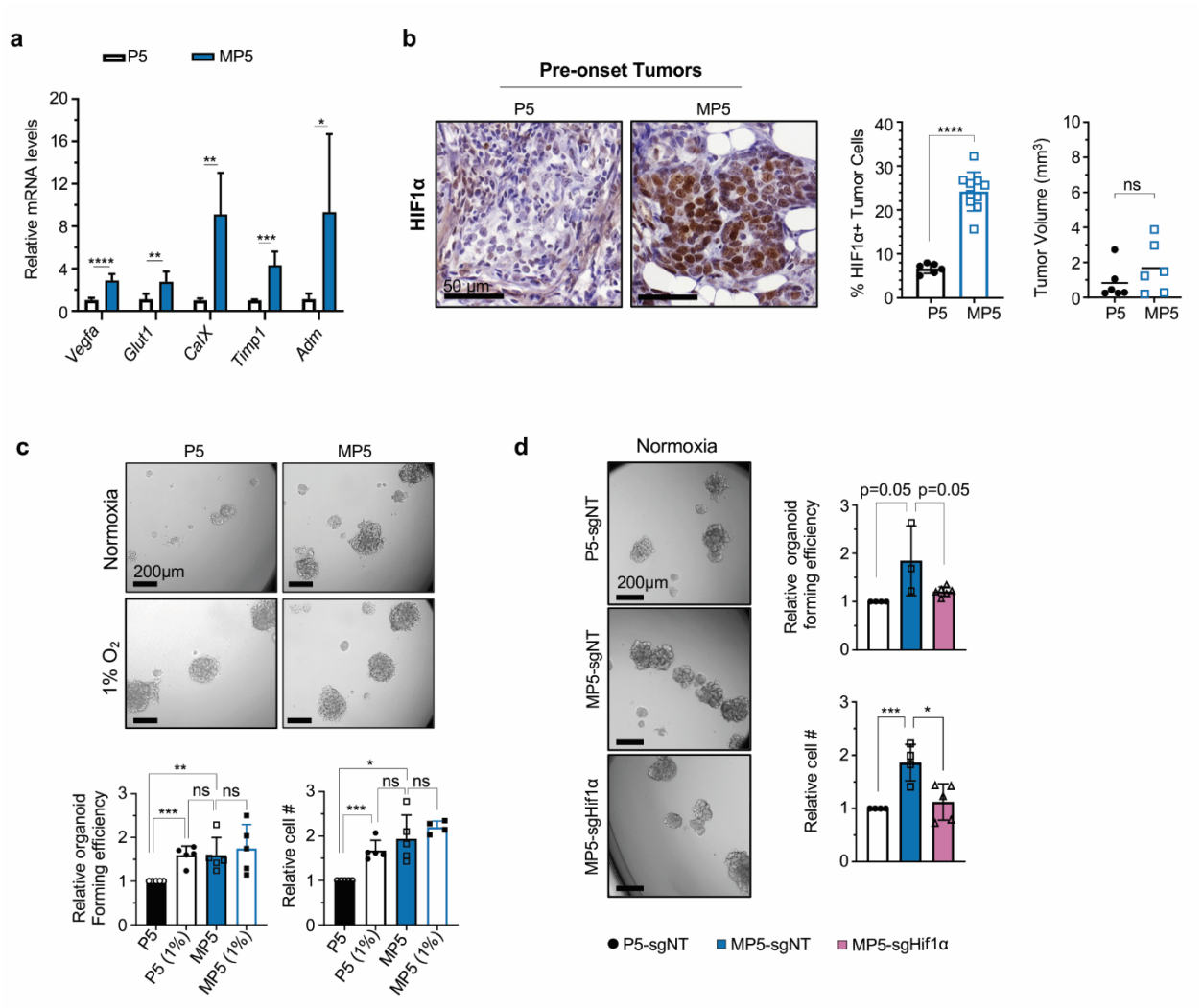

Figure 4. HIF1α upregulation in Mll3-mutant pre-onset nodules promote stem cell organoids and proliferation. (a) mRNA expression of HIF1α downstream targets in P5 and MP5 organoids from line #4. **(b)** Immunohistochemistry images and quantification of HIF1α expression in P5 pre-onset tumor nodules (n=6) compared to MP5 pre-onset tumor nodules (n=10) from line #1. Right graph shows tumor volumes of P5 and MP5 tumors analyzed for HIF1α expression. **(c)** Relative organoid forming efficiency and cell number comparison in P5 and MP5 organoids grown in normoxic and hypoxic culture (n=5 independent experiments). **(d)** Relative organoid forming efficiency and cell number comparison in P5-sg*NT* and MP5-sg*NT* and MP5-sg*HIF1α* organoids grown in normoxic culture (n=3-5 independent cultures).

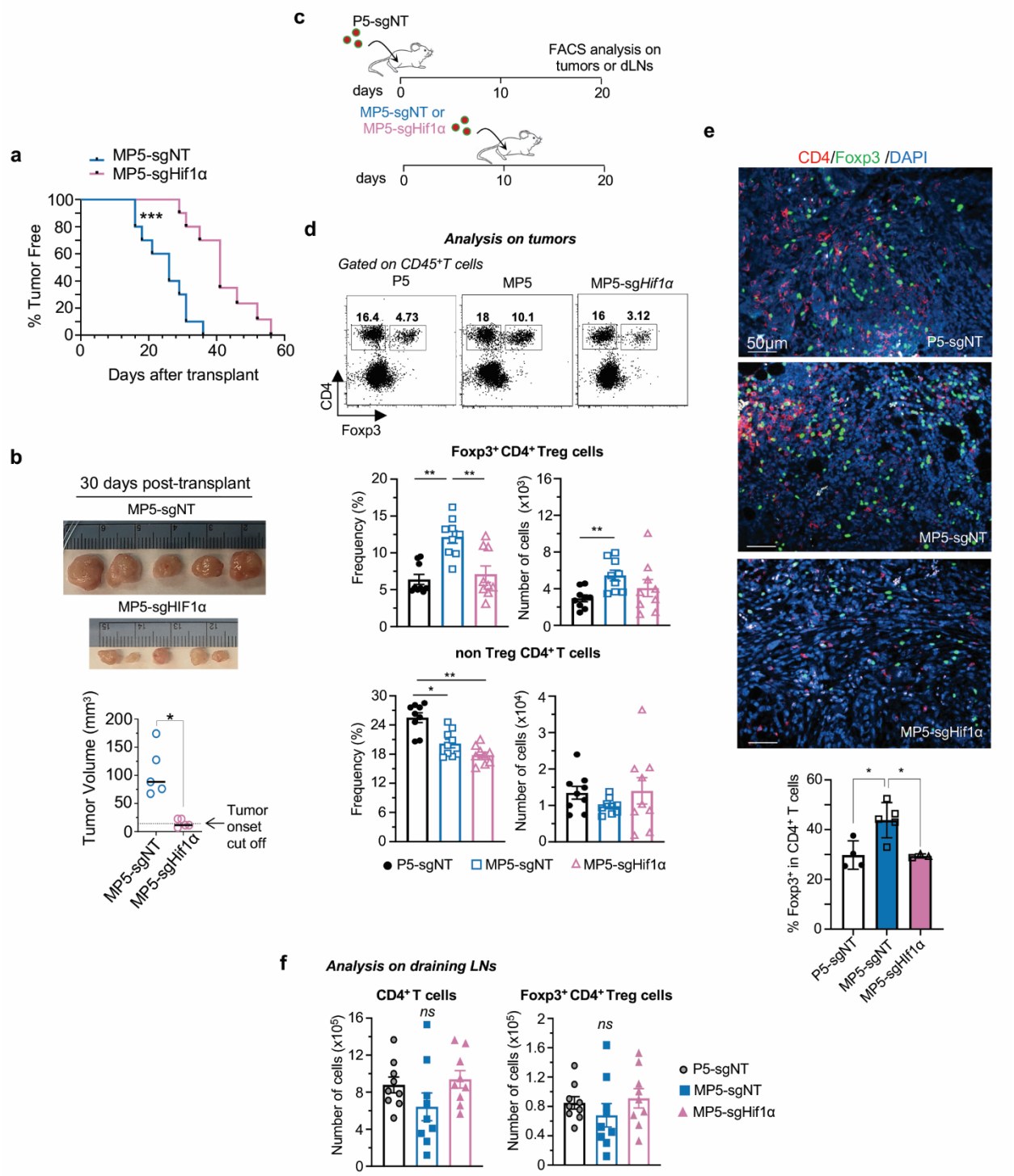

Figure 5. HIF-1α upregulation in Mll3-mutant tumors is required for early tumor onset and Treg cell infiltration. (a) Kaplan-Meier survival analysis of tumor onset for of MP5-sg*NT* tumors (n=10) compared to MP5-sg*Hif1a* tumors (n=10) transplanted to WT FVB mice. Pooled from two independent experiments. **(b)** Dissected tumor images and mean tumor volume comparison between MP5-sg*NT* (n=5) and MP5-sg*Hif1a* (n=5) tumors collected 30 days post-transplantation.

A centimeter ruler scale (with 1mm units) is included in the images. **(c)** Schematics of transplant and analysis strategy. FVB mice were transplanted with P5-sg*NT* and MP5-sg*NT* and MP5-sg*Hif1a* MaSCs. Twenty or 10 days post-transplant, tumors and draining LNs were extracted and analyzed by flow cytometry. **(d)** Representative dot plots of $CD4^+$ T and $CD4^+Foxp3^+$ T cells in pre-onset tumor nodules. Graphs show numbers and frequency pooled from 3 independent experiment (n=9 pre-onset tumor nodules). **(e)** Immunofluorescence images and quantification of CD4 and Foxp3 co-expression in P5-sg*NT* pre-onset tumor nodules (n=4) compared to MP5-sg*NT* pre-onset tumor nodules (n=5) and MP5-sg*Hif1α* pre-onset tumor nodules (n=3). **(f)** Graphs show the number of $CD4^+$ and $CD4^+Foxp3^+$ cells in draining LNs. Pooled from 3 independent experiment (n=9 samples/group). P-values (*< 0.05, **< 0.01, ***< 0.001 and ****< 0.0001) are indicated.

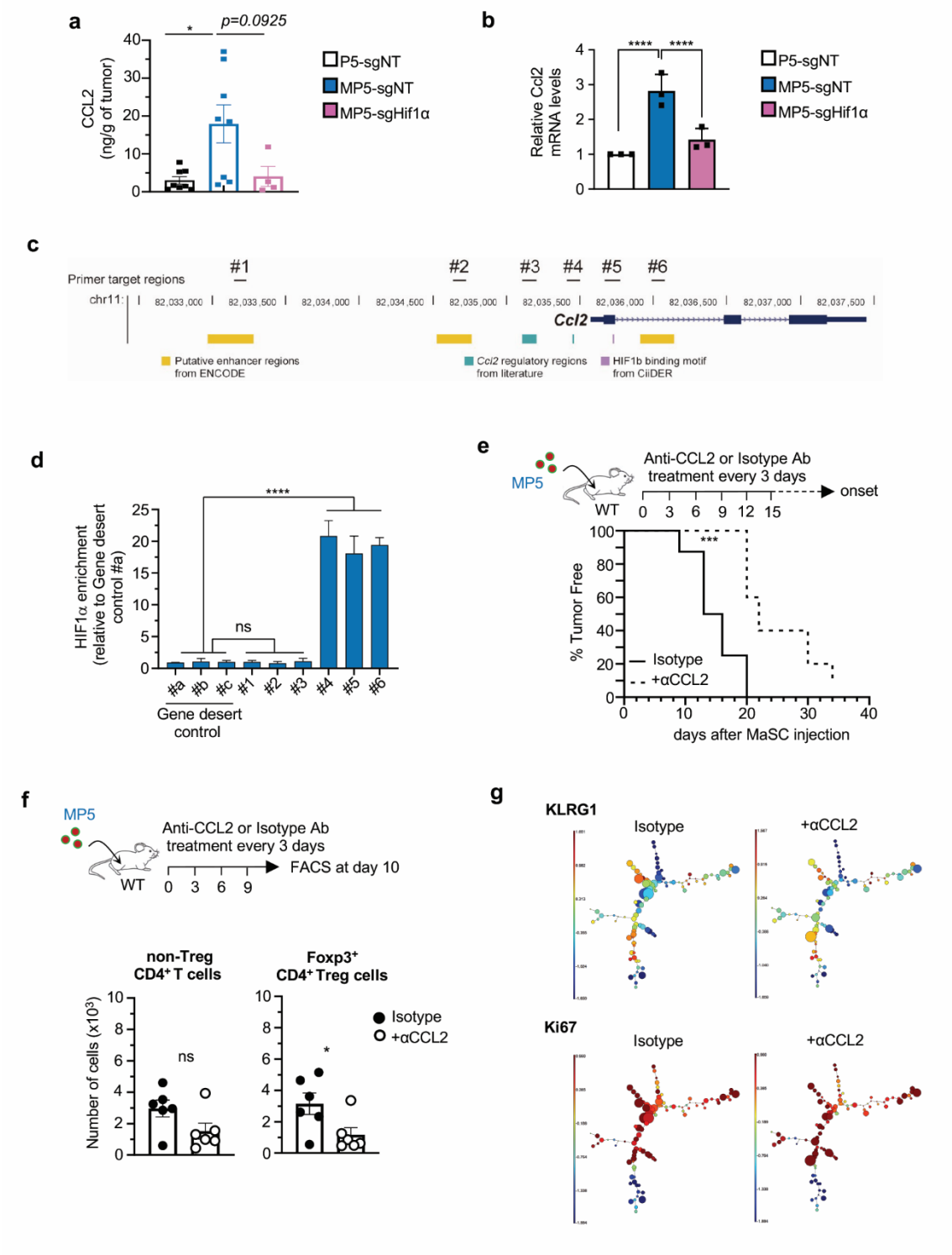

Figure 6. HIF1a mediates upregulation of CCL2 in tumor cells and CCL2 promotes Treg cell infiltration and early tumor onset. (a) Graph shows the quantity of CCL2 chemokine among P5-sg*NT*, MP5-sg*NT* and MP5-sg*HIF1α* pre-onset tumor nodules as depicted in Figure 5c. **(b)** *Ccl2* mRNA expression in P5-sg*NT*, MP5-sg*NT* and MP5-sg*Hif1a* organoid lines. **(c)** Putative regulatory regions and HIF binding sites at the *Ccl2* gene locus. Upper panel shows the genomic

regions analyzed by HIF1α ChIP-qPCR in (d). **(d)** Graph shows relative enrichment of HIF1α binding around the *Ccl2* transcription start site (TSS) in MP5 MaSCs (line #3). Gene desert regions were used as negative controls. Graph shows a representative result from 3 independent experiments. **(e)** WT mice were transplanted with MP5 MaSCs cells and after 3 days treated with anti-CCL2 or isotype Abs as indicated in the schematics. Kaplan-Meier survival analysis of tumor onset for MP5 tumors treated or not with anti-CCL2 Ab in a pool of 2 experiments (n=10 tumors/group). **(f)** Graphs show the frequency and numbers of $CD4^+Foxp3^+$Treg cells in MP5 pre-onset tumor nodules treated with anti-CCL2 Ab or not in a pool of 2 experiments (n=6 pre-onset tumor nodules). **(g)** FlowSOM representation for indicated markers on $Foxp3^+CD4^+$Treg cells from MP5 pre-onset tumor nodules treated or not with anti-CCL2 Ab. Each node is proportional to cell numbers and color scale is proportional to mean fluorescence intensity of indicated markers.

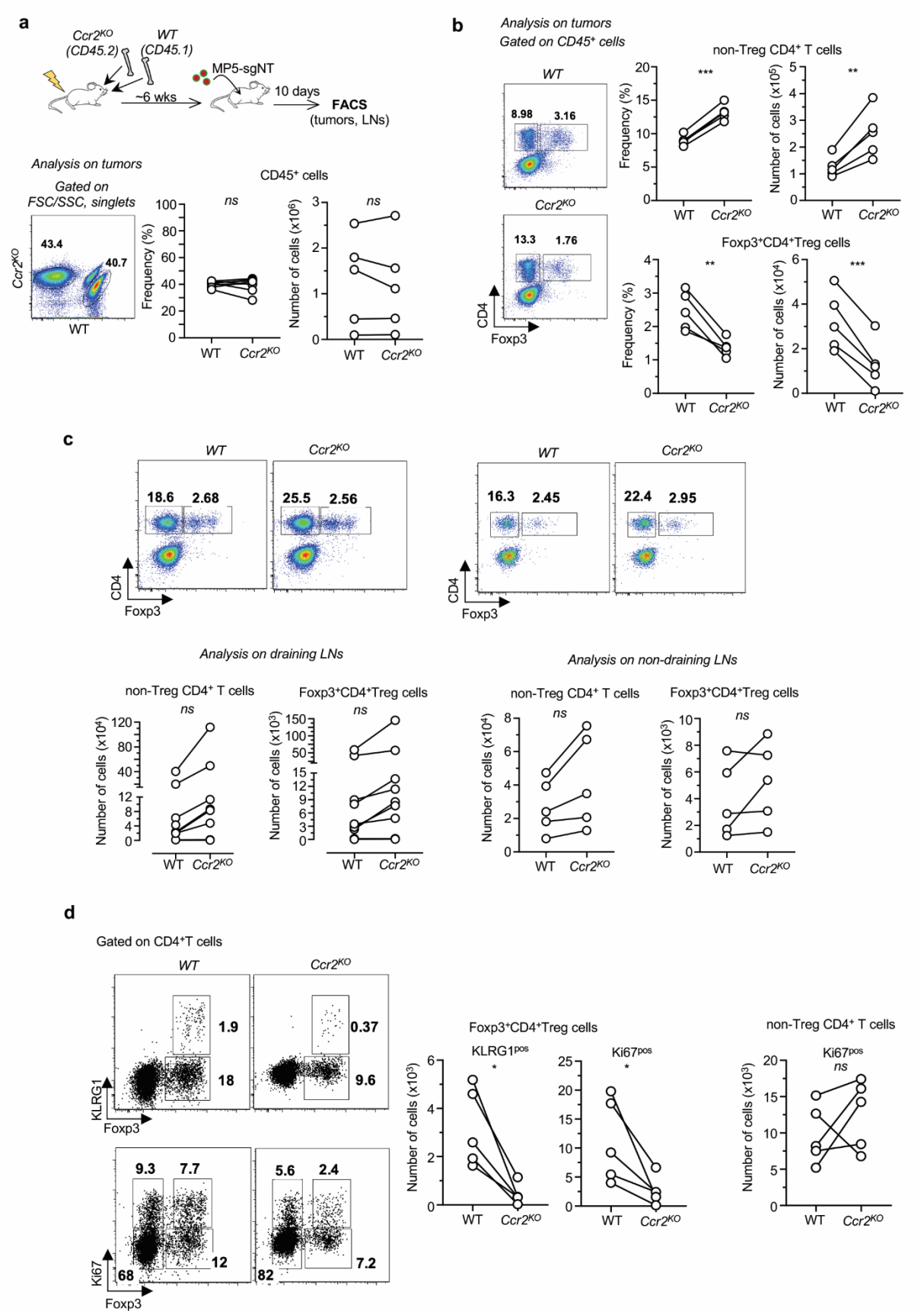
a
Ccr2KO (CD45.2)
WT (CD45.1)
~6 wks
MP5-sgNT
10 days
FACS (tumors, LNs)
Analysis on tumors
Gated on FSC/SSC, singlets
CD45+ cells
43.4
40.7
Ccr2KO
WT
Frequency (%)
Number of cells (x10^6)
ns
b
Analysis on tumors
Gated on CD45+ cells
non-Treg CD4+ T cells
Foxp3+CD4+Treg cells
8.98
3.16
13.3
1.76
CD4
Foxp3
Frequency (%)
Number of cells (x10^5)
Number of cells (x10^4)
c
18.6
2.68
25.5
2.56
16.3
2.45
22.4
2.95
Analysis on draining LNs
Analysis on non-draining LNs
Number of cells (x10^3)
d
Gated on CD4+T cells
1.9
18
0.37
9.6
KLRG1
Foxp3
9.3
7.7
12
68
5.6
2.4
7.2
82
Ki67
KLRG1pos
Ki67pos
WT
Ccr2KO

Figure 7. CCR2 contributes to Treg cell entry in pre-onset tumor nodules. (a) Lethally irradiated CD45.1$^{+/-}$ recipient mice were reconstituted with WT CD45.1$^{+/+}$ and *Ccr2^{KO}* CD45.2 BM. Six weeks post reconstitution, MP5-sgNT cells were transferred to mice and 10 days later, pre-onset tumor nodules and dLNs were collected for FACS analysis. Graphs show the immune cells frequency and numbers in WT and *Ccr2^{KO}* hematopoietic-derived (CD45^{+}) compartment of preonset nodules. **(b)** Graphs show non-Treg CD4^{+} T cells or Foxp3^{+}CD4^{+} Treg cells frequency and numbers in WT and *Ccr2^{KO}* compartments. Representative dot plots are shown. **(c)** Graphs show the number of non-Treg CD4^{+} T cells or Foxp3^{+}CD4^{+} Treg cells in dLNs and non-dLNs in WT and *Ccr2^{KO}* compartments. Representative dot plots are shown. **(d)** Graphs show the numbers of KLRG1^{+} and Ki67^{+} non-Treg CD4^{+} T cells or Foxp3^{+}CD4^{+} Treg cells in WT and *Ccr2^{KO}* compartments. Representative dot plots are shown. Each symbol corresponds to 1 individual mouse in 1 of 2 replicate experiment and representative dot plot are shown. P-values (*< 0.05, **< 0.01, ***< 0.001 and ****< 0.0001) are indicated.

Supplementary Figure Legends

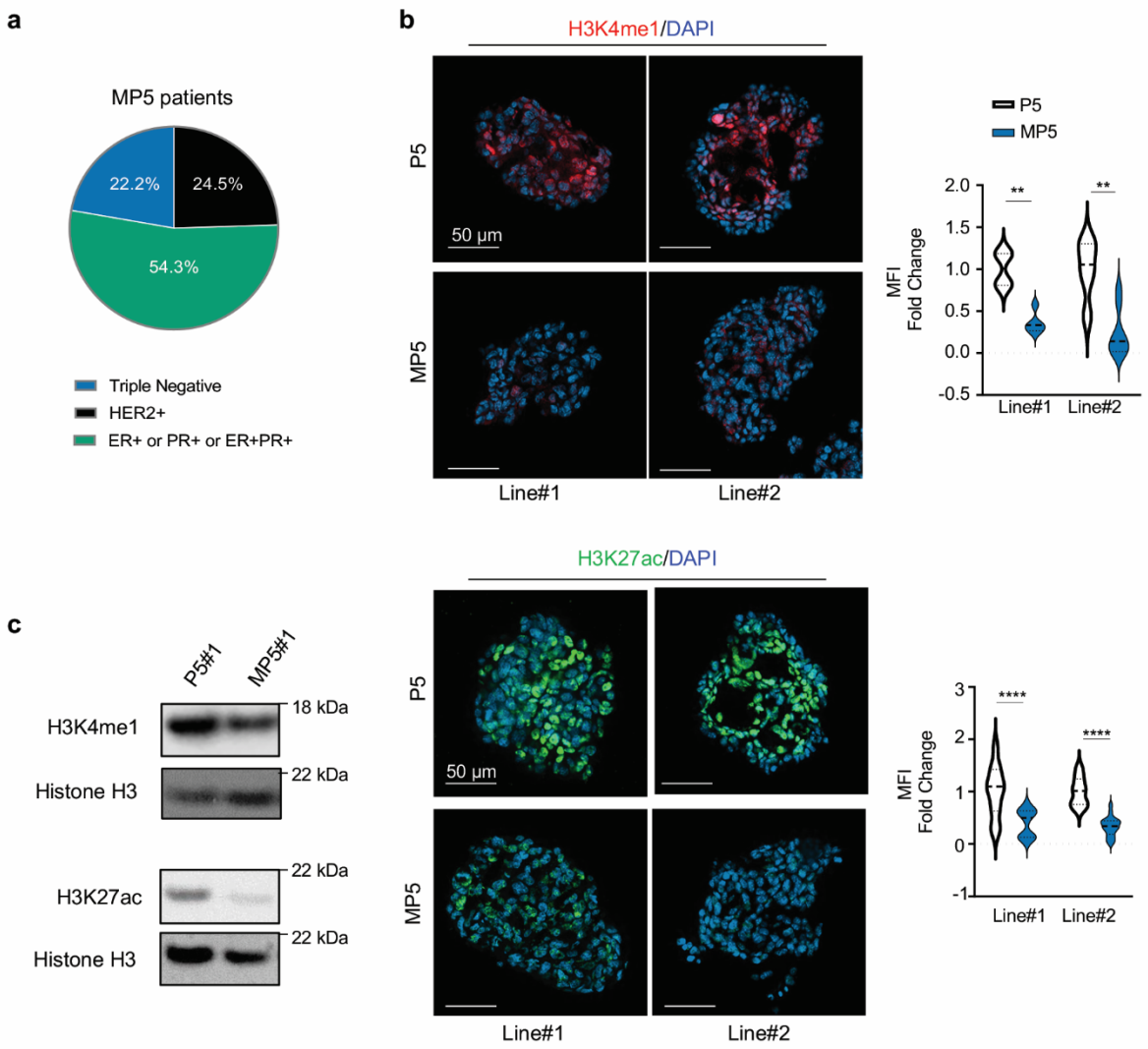

d

		Median Onset (Days)			Volume Doubling Time (Days)		
	Background	**P5**	**MP5**	**P value**	**P5**	**MP5**	**P value**
Line #1	Pik3ca^{H1047R}	128	39	**0.0019**	27.6	11.4	**<0.0001**
Line #3	Pik3ca^{H1047R}	76.5	41	**0.0005**	20.5	7.9	**<0.0001**
Line #4	Pik3ca^{H1047R}	51	25	**0.0002**	9.9	4.5	**<0.0001**
Line #2	Pik3ca*	51	32	**0.0191**	26.6	10.8	**<0.0001**
Line #7	Pik3ca*	61	22	**<0.0001**	15.9	3.3	**<0.0001**

Supplemental Figure 1, related to Figure 1. (a) Breast cancer subtype data analysis for patients with simultaneous PIK3CA/MLL3/TP53 mutations. Percentage of cases in each subtype was shown (n= 63; TCGA, MSKCC-IMPACT and METABRIC databases). **(b)** Immunofluorescence images and quantification of H3K4me1 (top) and H3K27ac (bottom) levels in P5 and MP5 organoids from lines #1 and #2 (n= 15-30 organoids). **(c)** Western blot analysis for H3K4me1 and

H3K27ac levels in P5 and MP5 organoids from line #1. **(d)** Medium tumor onset time and tumor growth rate for different pairs of P5 and MP5 tumors (lines #1-#4 and #7; n= 8-12 tumors per individual genotype and line). 300K single cells were injected per #4 gland. P-values (**$p < 0.01$ and ****$p < 0.0001$) are indicated.

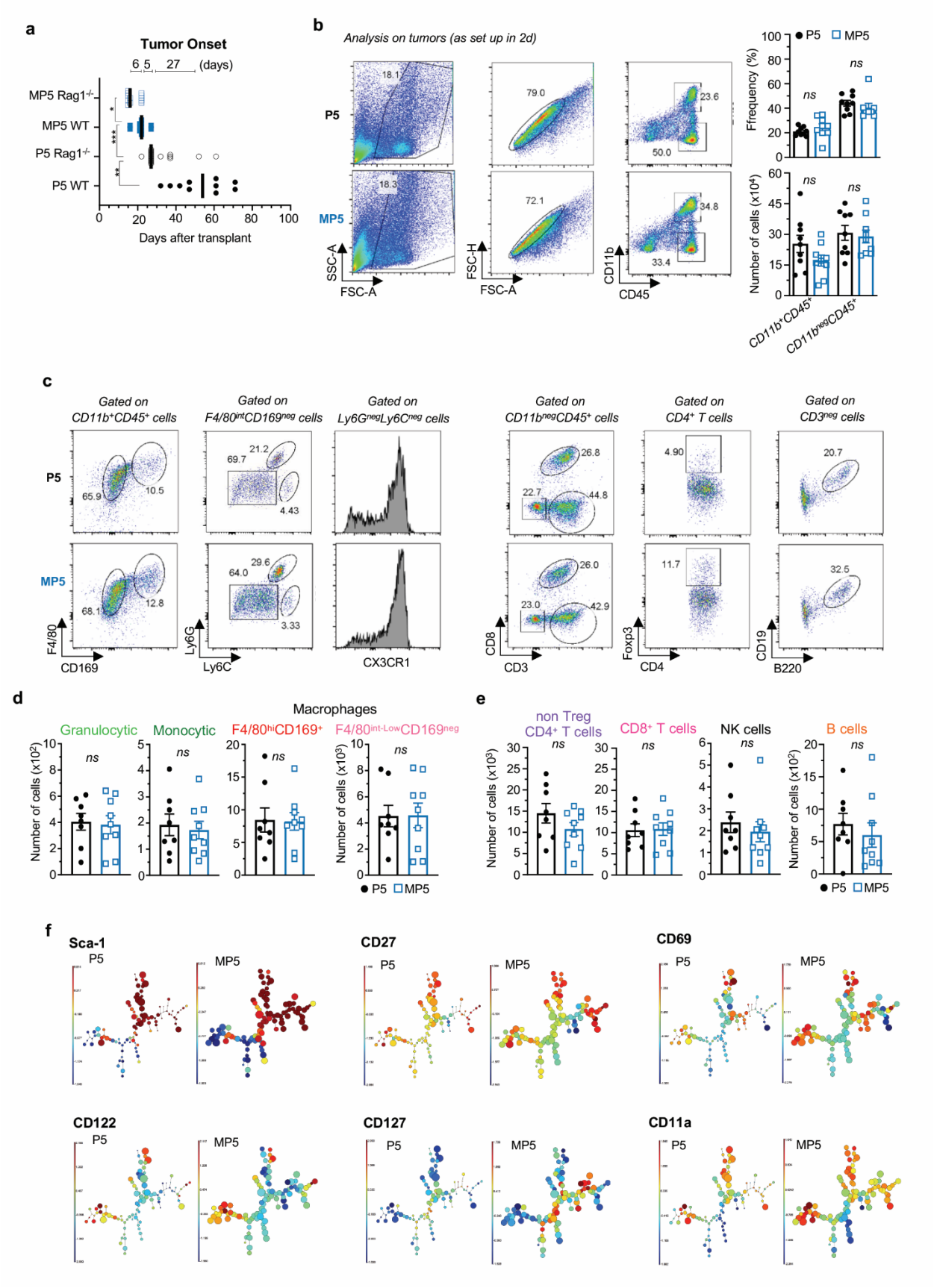
a
Tumor Onset
6 5 27 (days)
MP5 Rag1-/-
MP5 WT
P5 Rag1-/-
P5 WT
Days after transplant
b
Analysis on tumors (as set up in 2d)
P5
MP5
SSC-A
FSC-A
FSC-H
CD11b
CD45
Frequency (%)
Number of cells (x10⁴)
CD11b+CD45+
CD11bnegCD45+
c
Gated on CD11b+CD45+ cells
Gated on F4/80intCD169neg cells
Gated on Ly6GnegLy6Cneg cells
Gated on CD11bnegCD45+ cells
Gated on CD4+ T cells
Gated on CD3neg cells
F4/80
CD169
Ly6G
Ly6C
CX3CR1
CD8
CD3
Foxp3
CD4
CD19
B220
d
Macrophages
Granulocytic
Monocytic
F4/80hiCD169+
F4/80int-LowCD169neg
Number of cells (x10²)
Number of cells (x10³)
ns
P5
MP5
e
non Treg CD4+ T cells
CD8+ T cells
NK cells
B cells
f
Sca-1
CD27
CD69
CD122
CD127
CD11a

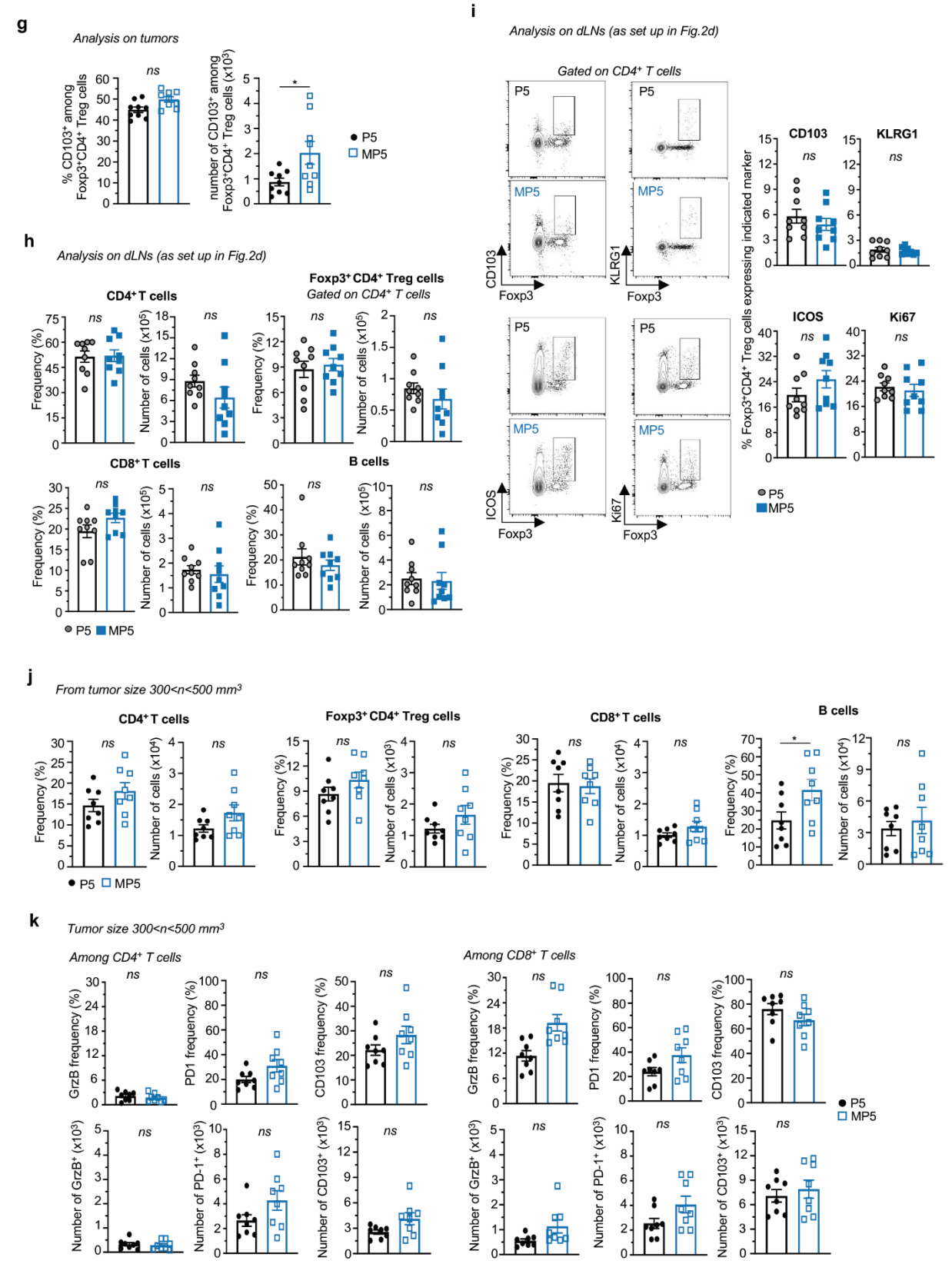
g
Analysis on tumors
% CD103+ among Foxp3+CD4+ Treg cells
number of CD103+ among Foxp3+CD4+ Treg cells (x10³)
ns
*
P5
MP5
h
Analysis on dLNs (as set up in Fig.2d)
CD4+ T cells
Foxp3+ CD4+ Treg cells
Gated on CD4+ T cells
CD8+ T cells
B cells
Frequency (%)
Number of cells (x10⁵)
P5 MP5
i
Analysis on dLNs (as set up in Fig.2d)
Gated on CD4+ T cells
CD103
KLRG1
ICOS
Ki67
Foxp3
% Foxp3+CD4+ Treg cells expressing indicated marker
j
From tumor size 300<n<500 mm³
CD4+ T cells
Foxp3+ CD4+ Treg cells
CD8+ T cells
B cells
Frequency (%)
Number of cells (x10⁴)
k
Tumor size 300<n<500 mm³
Among CD4+ T cells
Among CD8+ T cells
GrzB frequency (%)
PD1 frequency (%)
CD103 frequency (%)
Number of GrzB+ (x10³)
Number of PD-1+ (x10³)
Number of CD103+ (x10³)

Supplemental Figure 2, related to Figure 2. (a) Median tumor onset delay comparison between P5 tumors and MP5 tumors from line #7 transplanted to WT B6 mice and *Rag1*$^{-/-}$ mice (n=10-16 tumors per group, pooled from two independent experiments). **(b)** As depicted in Fig. 2d, graphs show the frequency and the number of CD11b^{+}CD45^{+} and CD11b^{neg}CD45^{+} cells in P5 and MP5 pre-onset tumor nodules. The gating strategy and representative dot plots are shown. Panels pool data from 2 independent replicate experiments (n=9 pre-onset tumor nodules). **(c)** Representative gating strategy to isolate immune cell subsets from CD11b^{+}CD45^{+} and CD11b^{neg}CD45^{+} cells in P5 and MP5 pre-onset tumor nodules. **(d, e)** Graphs show the number of indicated subsets. Panels pool from 2 independent replicate experiments (n=9 pre-onset tumor nodules). **(f)** FlowSOM representation for indicated markers on Foxp3^{+}CD4^{+}Treg cells from P5 and MP5 pre-onset tumor nodules. Each node is proportional to cell numbers and color scale is proportional to mean fluorescence intensity of indicated markers. **(g) Proportion of CD103+ Tregs in pre-onset tumors. (h, i)** Graphs show the frequency and the number of indicated immune cell subsets in dLNs in a pool from 2 independent replicate experiments (n=9 dLNs). Representative FACS dot plots of indicated marker expression of dLN Treg cells are shown. **(j)** Graphs show the frequency and the number of indicated immune cell subsets from 300-500 mm^{3} P5 and MP5 tumor size (n=8 tumors/group). **(k)** Graphs show the frequency and the number of GrzB^{+}, PD-1^{+} and CD103^{+} among CD4^{+} and CD8^{+} T cells in 300-500 mm^{3} tumors. P-values (*< 0.05, **< 0.01 and ***< 0.001) are indicated.

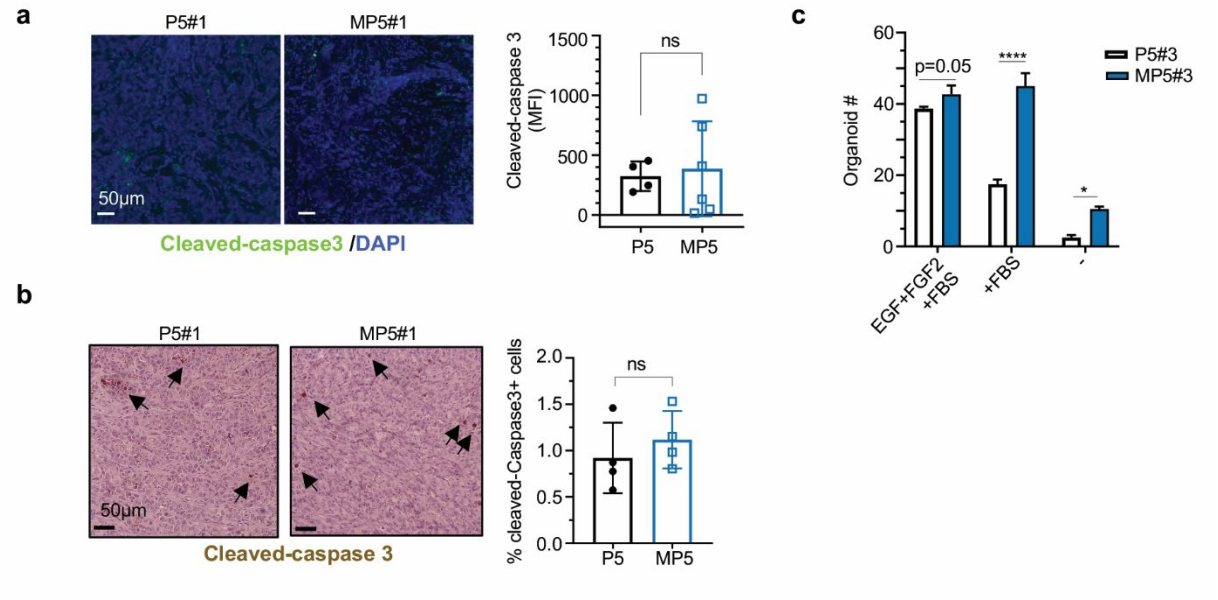

Supplemental Figure 3, related to Figure 3. (a) Immunofluorescence images and quantification of cleaved-caspase 3 expression in P5 pre-onset tumor nodules (n=4) compared to MP5 pre-onset tumor nodules (n=6) from line #3. **(b)** Immunohistochemistry images and quantification of cleaved-caspase 3 expression in P5 tumors (n=4) compared to MP5 tumors (n=4) from line #1; tumors were larger than 1000 mm^{3}. **(c)** Organoid-forming efficiency of P5 compared to MP5 MaSC line #3 in full organoid medium, no growth factor medium and no growth factor medium without serum. P-values (*p< 0.05, **p< 0.01, ***p< 0.001 and ****p< 0.0001) are indicated.

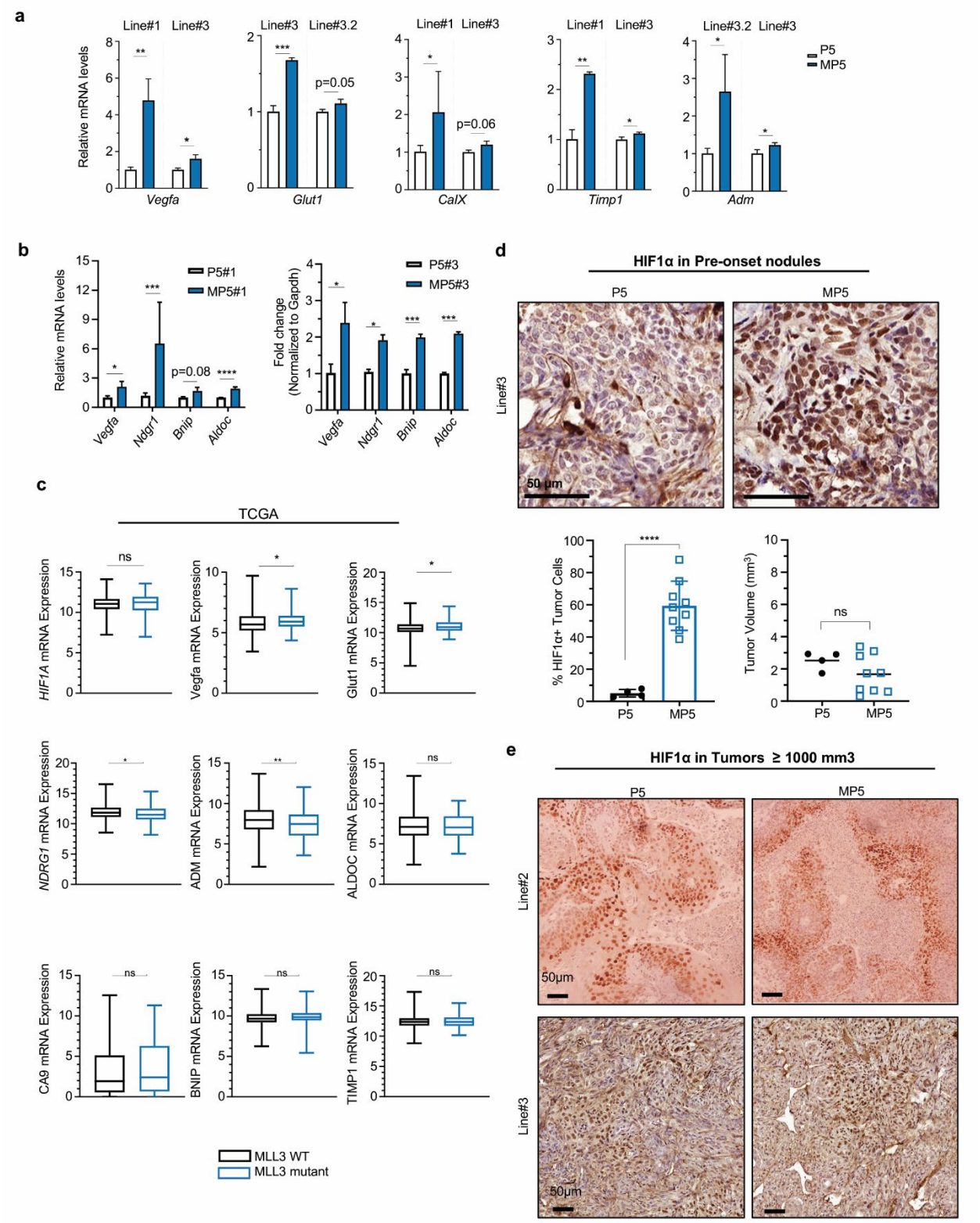

Supplemental Figure 4, related to Figure 4. (a) mRNA expression of HIF1α downstream targets in P5 and MP5 organoids from lines #1, #3 #3.1 or #3.2 in full medium. **(b)** mRNA expression of Hif1α downstream targets in P5 and MP5 organoids from line #1 and #3 in no growth factor

medium. **(c)** TCGA Breast Cancer database analysis of *HIF1A* and *HIF1A* downstream targets mRNA expression in MLL3-WT and MLL3-mutant patients. **(d)** Immunohistochemistry images and quantification of HIF1α expression in P5 pre-onset tumor nodules (n=4) compared to MP5 (n=9) pre-onset tumor nodules from line #3. Graph show the volume of tumor nodules used for HIF1α expression analysis. **(e)** Immunohistochemistry images and quantification of HIF1α expression in P5 tumors compared to MP5 tumors from line #2 and #3 (n= 4-5 tumors per line, tumors >1000mm^3).

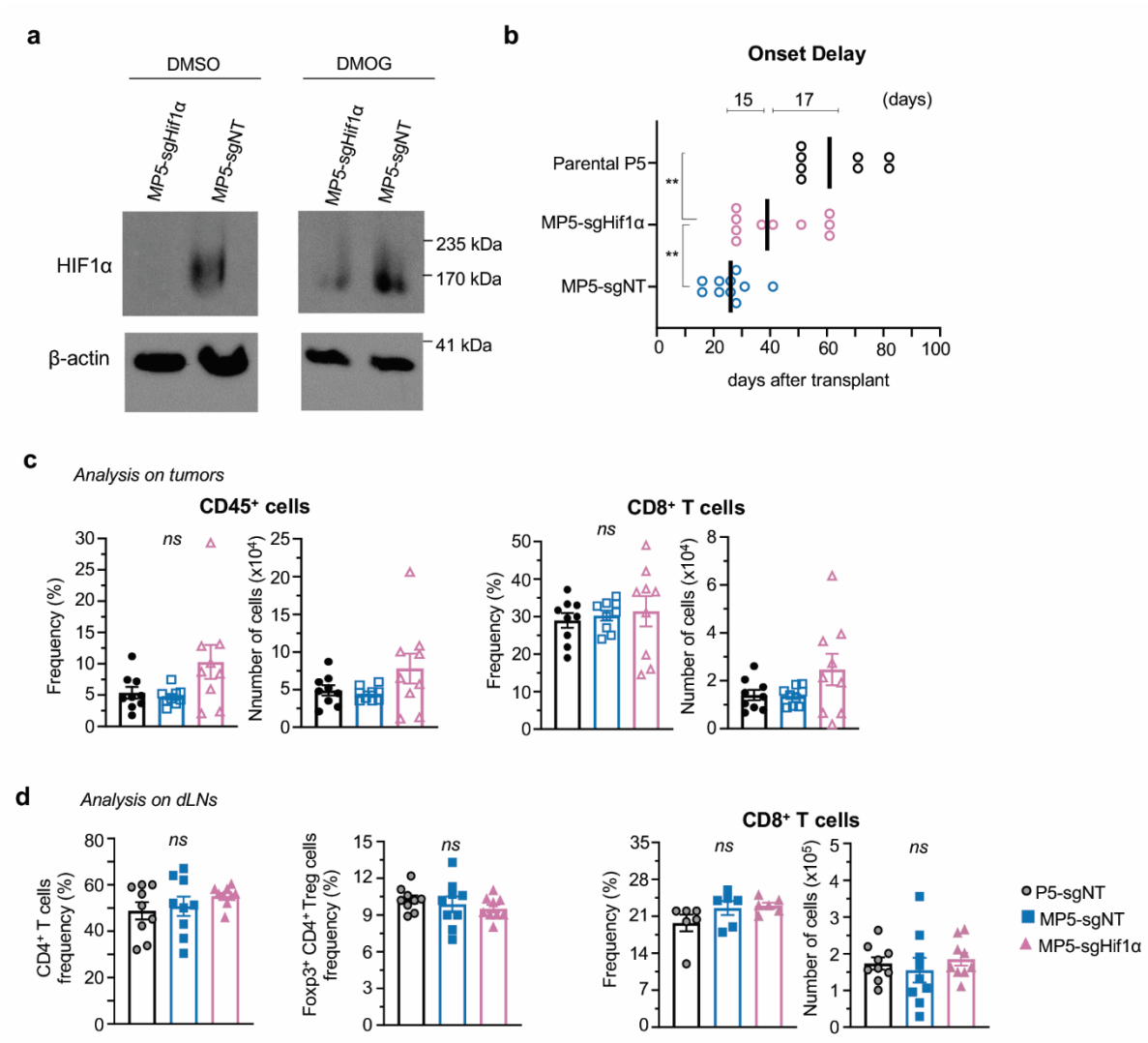

Supplemental Figure 5, related to Figure 5. (a) Western blot analysis of HIF1α expression in MP5-sg*NT* and MP5-sg*Hif1α* organoids in DMSO control or DMOG supplemented culture. **(b)** Median tumor onset delay comparison between P5 tumors from the parental cells (n=8), MP5-sg*NT* tumors (n=10) and MP5-sg*Hif1α* tumors (n=10), pooled from two independent experiments. **(c)** Graphs show the number of cells per sample and frequency and number of CD45$^+$ and CD8$^+$ T cells in P5, MP5-sg*NT* and MP5-sg*Hif1α* pre-onset tumor nodules. Data are pooled from 3 independent experiment (n=9 samples/group). **(d)** Graphs show the frequency of CD4$^+$ T and

CD4$^+$Foxp3$^+$ Treg cells and frequency and number of CD8$^+$ T cells in dLNs. Data are pooled from 3 independent experiment (n=9 samples/group). P-values (*< 0.05, and **< 0.01) are indicated.

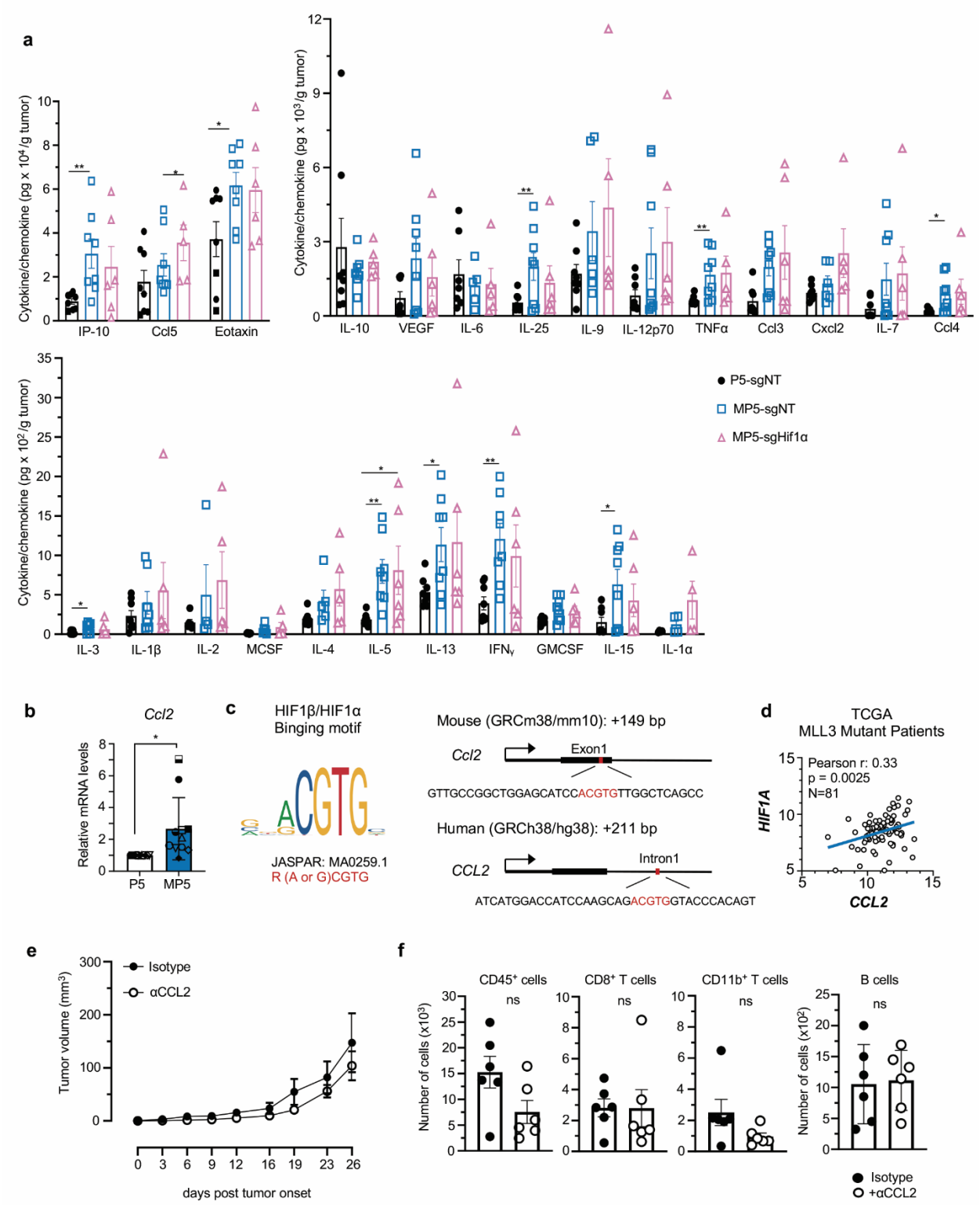

Supplemental Figure 6, related to Figure 6. (a) Quantification of levels of chemokines (CCL2, CCL3, CCL4, CCL5, CXCL2, CXCL10 and Eotaxin), cytokines (IL-1α, IL-1β, IL-6, IL-12p70, IFNγ, TNFα, IL-4, IL-5, IL-13, IL-25, IL-9, IL-2, IL-7, IL-15, IL-10 and IL-3) and growth factors (GMCSF, MCSF and VEGF) in P5-sgNT, MP5-sgNT and MP5-sgHIF1α pre-onset nodules as depicted in Figure 5c. **(b)** CCL2 mRNA expression in P5 and MP5 organoid lines #1, #2, #3, #4, and #7. **(c)** Hif1 beta/alpha binding motif (Hypoxia response element, HRE). Motif sequence is referred from JASPAR database. This motif is conserved around *Ccl2* transcription start site in both human and mouse. **(d)** TCGA Breast Cancer database analysis of HIF1a and CCL2 gene expression correlation in MLL3-mutant patients (n=81). **(e)** Graph represents MP5 tumor growth as depicted in Figure 6e in a pool of 2 experiments (n=10 tumors/group). **(f)** Graphs show the number of $CD45^+$ cells, $CD8^+$ T cells, non-Treg $CD4^+$ T cells and B cells in MP5 pre-onset tumor nodules treated with anti-CCL2 or not in a pool of 2 experiments (n=6 pre-onset tumor nodules). P-values (*< 0.05, **< 0.01 and ***< 0.001) are indicated.

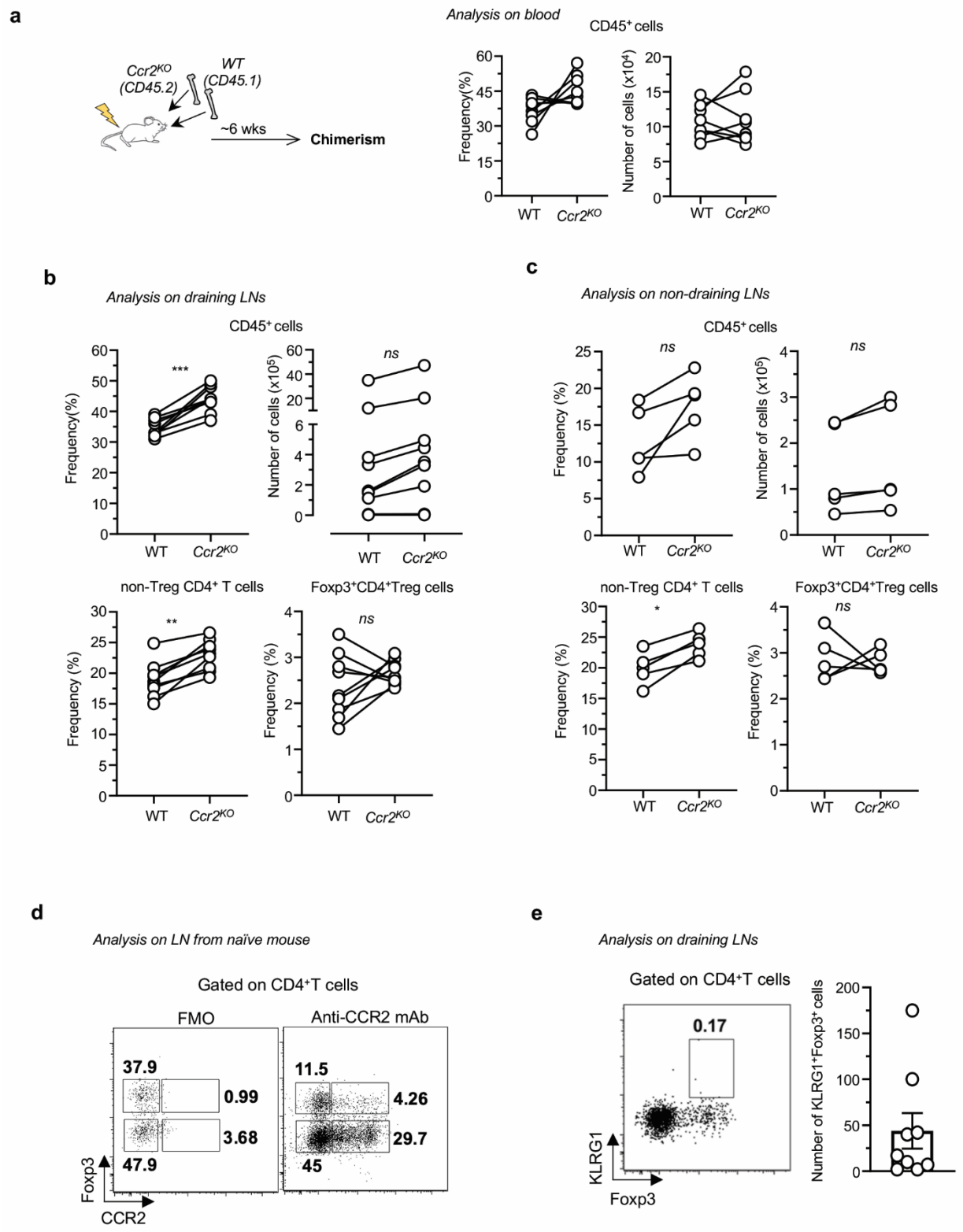

Supplemental Figure 7, related to Figure 7. (a) Analysis of chimerism in the blood of mixed-BM chimeras, as depicted in Figure 7a. Graphs show hematopoietic-derived ($CD45^+$) cell frequency and numbers in compartments of mixed BM chimeras. **(b, c)** Graphs show

hematopoietic-derived ($CD45^+$) cell frequency and numbers, and that of non-Treg $CD4^+$ T cells or $Foxp3^+CD4^+$ Treg cells in dLNs (b) and non-dLNs (c) in WT and *Ccr2*^{KO} compartments. **(d)** CCR2 expression on non-Treg $CD4^+$ T cells or $Foxp3^+CD4^+$ Treg cells from naïve mouse LNs. **(e)** KLRG1 expression on $Foxp3^+CD4^+$ Treg cells from LNs. Representative dot plot are shown (d, e) and graphs represents the number of $KLRG1^+Foxp3^+$ $CD4^+$ Treg cells.